



ATLAS Note

GROUP-2017-XX



9th November 2020

Draft version 0.1

1

2 **A Deep Learning Approach to Differential**
3 **Measurements of Higgs - Top Interactions in**
4 **Multilepton Final States**

5

The ATLAS Collaboration

6 Several theories Beyond the Standard Model modify the momentum spectrum of the Higgs
7 Boson, without significantly altering the overall rate of Higgs produced from top quark pairs.
8 A differential measurement of the Higgs transverse momentum provides a way to search for
9 these effects at the LHC. Because of the challenges inherent to reconstructing the Higgs in
10 multilepton final states, a deep learning approach is used to predict the momentum spectrum
11 of the Higgs for events where the Higgs Boson is produced from top quark pairs and decays
12 to final states that include multiple leptons. The regressed Higgs p_T is fit to data for events
13 with two or three leptons in the final state, and estimates of the sensitivity to variations in the
14 Higgs p_T spectrum are given.

© 2020 CERN for the benefit of the ATLAS Collaboration.

15 Reproduction of this article or parts of it is allowed as specified in the CC-BY-4.0 license.

16 **Contents**

17	I Introduction	6
18	1 Introduction	6
19	II Theoretical Motivation	8
20	2 The Standard Model and the Higgs Boson	8
21	2.1 The Forces and Particles of the Standard Model	9
22	2.2 The Higgs Mechanism	11
23	2.2.1 The Higgs Field	12
24	2.2.2 Electroweak Symmetry Breaking	14
25	2.3 Limitations of the Standard Model	16
26	3 Effective Field Theory in $t\bar{t}H$ Production	17
27	3.1 Extensions to the Higgs Sector	17
28	3.2 Six Dimensional Operators	17
29	III The LHC and the ATLAS Detector	18
30	4 The LHC	18
31	5 The ATLAS Detector	21
32	5.1 Inner Detector	22
33	5.2 Calorimeters	23
34	5.3 Muon Spectrometer	24
35	5.4 Trigger System	25
36	IV Search for Dimension-Six Operators	26
37	6 Data and Monte Carlo Samples	26
38	6.1 Data Samples	27
39	6.2 Monte Carlo Samples	28
40	7 Object Reconstruction	28
41	7.1 Trigger Requirements	29
42	7.2 Light Leptons	29
43	7.3 Jets	30
44	7.4 Missing Transverse Energy	31
45	8 Higgs Momentum Reconstruction	31

46	8.1	Decay Candidate Reconstruction	32
47	8.2	b-jet Identification	33
48	8.2.1	2lSS Channel	34
49	8.2.2	3l Channel	37
50	8.3	Higgs Reconstruction	41
51	8.3.1	2lSS Channel	42
52	8.3.2	3l Semi-leptonic Channel	44
53	8.3.3	3l Fully-leptonic Channel	47
54	8.4	p_T Prediction	49
55	8.4.1	2lSS Channel	51
56	8.4.2	3l Semi-leptonic Channel	52
57	8.4.3	3l Fully-leptonic Channel	53
58	8.5	3l Decay Mode	55
59	9	Signal Region Definitions	56
60	9.1	Pre-MVA Event Selection	56
61	9.2	Event MVA	59
62	9.3	Signal Region Definitions	64
63	9.3.1	2lSS	67
64	9.3.2	3l – Semi – leptonic	67
65	9.3.3	3l – Fully – leptonic	67
66	10	Background Rejection MVA	67
67	10.1	Background Rejection MVAs	67
68	10.1.1	2lSS - High p_T	68
69	10.1.2	2lSS - Low p_T	69
70	10.1.3	3l Semi-Leptonic - High p_T	69
71	10.1.4	3l Semi-Leptonic - Low p_T	69
72	10.1.5	3l Fully Leptonic - High p_T	69
73	10.1.6	3l Fully Leptonic - Low p_T	69
74	11	Systematic Uncertainties	69
75	12	Results	71
76	12.1	Results - 80 fb^{-1}	71
77	12.2	Projected Results - 140 fb^{-1}	73
78	V	Conclusion	74
79	Appendices		76
80	A	Machine Learning Models	76
81	A.1	Alternate b-jet Identification Algorithm	76

82	A.1.1	Binary Classification of the Higgs p_T	77
83	A.1.2	Impact of Alternative Jet Selection	77
84	A.1.3	Background Rejection MVAs	78

Part I**Introduction****1 Introduction**

Particle physics is an attempt to describe the fundamental building blocks of the universe and their interactions. The Standard Model (SM) - our best current theory of fundamental particle physics - does a remarkable job of that. All known fundamental particles and (almost) all of the forces underlying their interactions can be explained by the SM, and the predictions from this theory agree with experiment to an incredibly precise degree. This is especially true since the Higgs Boson, the last piece of the SM predicted decades before, was finally discovered at the Large Hadron Collider (LHC) in 2012.

Despite the success of the SM, there remains significant work to be done. For one, the SM is incomplete: it fails to provide a description of gravity, to give an explanation for the observation of Dark Matter, or to provide a mechanism for neutrinos to gain mass. Further, a Higgs Boson with a mass of around 125 GeV, as observed at the LHC, gives rise to what is known a hierarchy problem - such a low mass Higgs requires a seemingly unnatural level of “fine tuning” that is unexplained by the SM.

A promising avenue for addressing these problems is to study the properties of the Higgs Boson and the way it interacts with other particles, in part simply because these interactions

103 have not been measured before. Its interactions with the Top Quark are a particularly promising
104 place to look. Because the Higgs Field is responsible for allowing particle to acquire mass, the
105 strength of a particle's interaction with the Higgs Boson is proportional to its mass. As the most
106 massive of the fundamental particles, the Top Quark has the strongest coupling to the Higgs
107 Boson, meaning any new physics in the Higgs sector is likely to present itself most prominently
108 in its interaction with the Top Quark.

109 These interactions can be measured by directly by studying the production of a Higgs
110 Boson in association with a pair of Top Quarks ($t\bar{t}H$). While studies have been done measuring
111 the overall rate of $t\bar{t}H$ production, there are several theories of physics Beyond the Standard
112 Model (BSM) that would affect the kinematics of $t\bar{t}H$ production without altering its overall
113 rate. This dissertation attempts to make a differential measurement of the kinematics of the
114 Higgs Boson in $t\bar{t}H$ events in order to search for these BSM effects.

115 An Effective Field Theory model can be used to model the low energy effects of high
116 energy physics.

117 The proton-proton collision data collected by the ATLAS detector at the LHC from 2015-
118 2018 provides the opportunity to make this measurement for the first time. The unprecedented
119 energy achieved by the LHC during this period greatly increase the rate at which $t\bar{t}H$ events are
120 produced, and the large amount of data collected provides the necessary statistics for a differential
121 measurement to be performed.

122 A study of $t\bar{t}H$ events with multiple leptons in the final state is performed, using 139 fb^{-1}

123 of data from proton-proton collisions at an energy $\sqrt{s} = 13$ TeV collected by the ATLAS detector
124 from 2015-2018. Events are separated into channels based on the number of light leptons in the
125 final state - either two same-sign leptons, or three leptons. A deep neural network is used to
126 reconstruct the momentum of the Higgs Boson in each event. This momentum spectrum is fit to
127 data for each analysis channel, the result of which is used to place limits on BSM effects.

128 This dissertation begins with a brief explanation of the SM, its limitations, and the theor-
129 etical motivation behind this work. This is followed by a description of the LHC and the ATLAS
130 detector. The analysis strategy is then described, and the results are presented. Finally, the results
131 of the study are summarized in the conclusion.

132 Part II

133 Theoretical Motivation

134 **2 The Standard Model and the Higgs Boson**

135 The Standard Model of particle physics (SM) is a Quantum Field Theory (QFT) describing the
136 known fundamental particles and their interactions. It accounts for three of the four known
137 fundamental force - electromagnetism, the weak nuclear force, and the strong nuclear force, but
138 not gravity. Further, the SM describes a mechanism for combining the weak and electromagnetic
139 forces into a singular interaction, known as the electroweak force. It is a non-Abelian gauge

¹⁴⁰ theory, invariant under the Lie Group $SU(3)_C \otimes SU(2)_L \otimes U(1)_Y$, where C refers to color
¹⁴¹ charge, L, the helicity of the particle, and Y, the hypercharge.

¹⁴² 2.1 The Forces and Particles of the Standard Model

¹⁴³ The SM particles, summarized in figure 2.1, can be classified into two general categories based
¹⁴⁴ on their spin: fermions, and bosons.

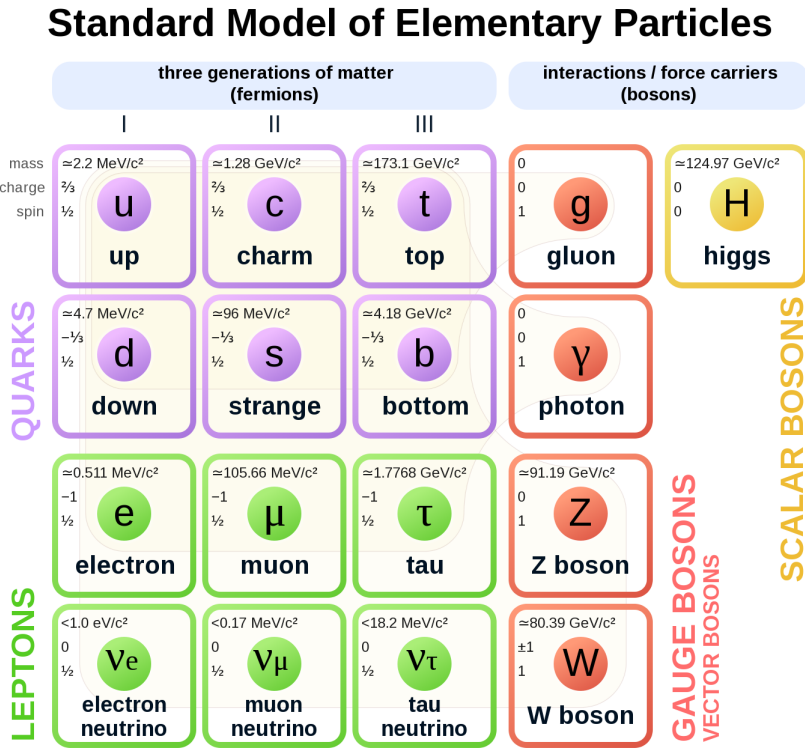


Figure 2.1: A summary of the particles of the Standard Model, including their mass, charge and spin, with the fermions listed on the left, and the bosons on the right. []

¹⁴⁵ Fermions are particles with $\frac{1}{2}$ -integer spin, which according to the spin-statistics theorem,
¹⁴⁶ causes them to comply with the Pauli-exclusion principle []. They can be separated into two

¹⁴⁷ groups, leptons and quarks, each of which consist of three generations of particles with increasing

¹⁴⁸ mass.

¹⁴⁹ Leptons are fermions interact via the electroweak force, but not the strong force. The three

¹⁵⁰ generation of leptons consist of the electron and electron neutrino, the muon and muon neutrino,

¹⁵¹ the tau and tau neutrino. The quarks, which do interact via the strong force - which is to say they

¹⁵² have color charge - in addition to the electroweak force. The three generations include the up

¹⁵³ and down quarks, the strange and charm quarks, and the top and bottom quarks. Each of these

¹⁵⁴ generations form left-handed doublets invariant under SU(2) transformations. For the leptons

¹⁵⁵ these doublets are:

$$\begin{pmatrix} e^- \\ \nu_e \end{pmatrix}_L, \begin{pmatrix} \mu^- \\ \nu_\mu \end{pmatrix}_L, \begin{pmatrix} \tau^- \\ \nu_\tau \end{pmatrix}_L \quad (2.1)$$

¹⁵⁶ And for the quarks:

$$\begin{pmatrix} u \\ d \end{pmatrix}_L, \begin{pmatrix} s \\ c \end{pmatrix}_L, \begin{pmatrix} t \\ b \end{pmatrix}_L \quad (2.2)$$

¹⁵⁷ For both leptons and quarks, the heavier generations can decay into the lighter generation

¹⁵⁸ of particles, while the first generation does not decay. Hence, ordinary matter generally consists

¹⁵⁹ of this first generation of fermions - electrons, up quarks, and down quarks. Each of these

¹⁶⁰ fermions has a corresponding anti-particle, which has an equal mass as its partner but opposite

¹⁶¹ charge. The fermions acquire their mass via the Higgs Mechanism, except for the neutrinos,

¹⁶² whose mass has been experimentally confirmed but is not accounted for in the SM.

¹⁶³ Bosons, by contrast, have integer spin, and are therefore unconstrained by the Pauli-

¹⁶⁴ exclusion principle. The SM includes two kinds of bosons: Gauge bosons, which are spin-1

¹⁶⁵ particles that mediate the interactions between the fermions, and a single scalar, i.e. spin-0,

¹⁶⁶ particle - the Higgs Boson. Of the gauge bosons, the W^+ , W^- and Z bosons - which are the

¹⁶⁷ mass eigenstates of the electroweak bosons - mediate the weak interaction, while the photon

¹⁶⁸ mediates the electric force, and the gluon mediates the strong force.

¹⁶⁹ 2.2 The Higgs Mechanism

¹⁷⁰ A key feature of the SM is the gauge invariance of its Lagrangian. However, any terms added to

¹⁷¹ the Lagrangian giving mass to the the gauge bosons would violate the underlying symmetry of

¹⁷² the theory. This presents a clear problem with the theory: The experimental observation that the

¹⁷³ W and Z bosons have mass seems to contradict the basic structure of the SM.

¹⁷⁴ Rather than abandoning gauge invariance, an alternative way for particles to acquire mass

¹⁷⁵ beyond adding a simple mass term to the Lagrangian was theorized by Higgs, Englert and Brout

¹⁷⁶ in 1964 []. This procedure for introducing masses for the gauge bosons while preserving local

¹⁷⁷ gauge invariance, known as the Higgs mechanism, was incorporated into the electroweak theory

¹⁷⁸ by Weinberg in 1967 [].

¹⁷⁹ **2.2.1 The Higgs Field**

¹⁸⁰ The Higgs mechanism introduces a complex scalar $SU(2)$ doublet, Φ , with the form:

$$\Phi = \begin{pmatrix} \phi^+ \\ \phi^0 \end{pmatrix}_L \quad (2.3)$$

¹⁸¹ This field introduces a scalar potential to the Lagrangian of the form:

$$V(\Phi) = \mu^2 |\Phi^\dagger \Phi| + \lambda (|\Phi^\dagger \Phi|)^2 \quad (2.4)$$

¹⁸² Where μ and λ are free parameters of the new field. This represents the most general
¹⁸³ potential allowed while preserving $SU(2)_L$ invariance and renormalizability. In the case that
¹⁸⁴ $\mu^2 < 0$, this potential takes the form shown in figure 2.2.

¹⁸⁵ The significant feature of this potential is that its minimum does not occur for a value of
¹⁸⁶ $\Phi = 0$. Instead, it is minimized when $|\Phi^\dagger \Phi| = -\mu^2/\lambda$. This means that in its ground state, the
¹⁸⁷ Higgs field takes on a non-zero value - referred to as a vacuum expectation value (VEV). So while
¹⁸⁸ the Higgs potential is globally symmetric, about the minimum this symmetry is broken. Since

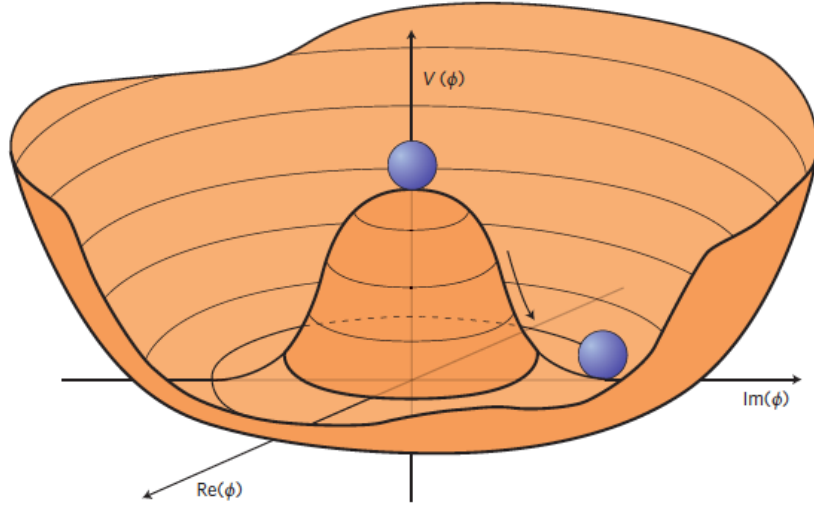


Figure 2.2: The value of the Higgs potential, $V(\Phi)$ as a function of Φ , for the case that $\mu^2 < 0$ [].

¹⁸⁹ the minimum is determined only by $\Phi^\dagger \Phi$, there is some ambiguity in the particular definition of
¹⁹⁰ the VEV, but it is generally represented as

$$\langle \Phi \rangle = \frac{1}{\sqrt{2}} \begin{pmatrix} 0 \\ v \end{pmatrix} \quad (2.5)$$

¹⁹¹ The full value of Φ can be written as

$$\langle \Phi \rangle = \frac{1}{\sqrt{2}} \begin{pmatrix} 0 \\ v + H/\sqrt{2} \end{pmatrix} \quad (2.6)$$

¹⁹² with v being the value of the VEV, and H being the real value of the scalar field.

193 **2.2.2 Electroweak Symmetry Breaking**

194 The Electroweak (EWK) interaction is described in the SM by a $SU(2)_L \otimes U(1)_Y$ gauge theory.
 195 This theory predicts three $SU(2)_L$ gauge boson, $W_\mu^1, W_\mu^2, W_\mu^3$, and a single $U(1)_Y$ gauge boson,
 196 B_μ . The couplings of these bosons to the Higgs field show up in the kinetic terms of the scalar
 197 field Φ in the Lagrangian:

$$(D_\mu \Phi)^\dagger (D^\mu \Phi) = |(\partial_\mu - \frac{ig}{2} W_\mu^a \sigma^a - \frac{ig'}{2} B_\mu Y) \phi|^2 \quad (2.7)$$

198 Here D_μ represents the covariant derivative required to preserve gauge invariance, g and
 199 g' represent coupling constant of the gauge bosons, σ^a denotes the Pauli matrices of $SU(2)$,
 200 and Y represents the hypercharge of $U(1)$. The terms in this interaction which contribute to the
 201 masses of the gauge bosons can be written as:

$$\frac{1}{2}(0, v)(\frac{g}{2} W_\mu^a \sigma^a - \frac{g'}{2} B_\mu)^2 \begin{pmatrix} 0 \\ v \end{pmatrix} \quad (2.8)$$

202 Expanding these terms into the mass eigenstates of the electroweak interaction yields four
 203 physical gauge bosons, two charged and two neutral, which are linear combinations of the fields

²⁰⁴ $W_\mu^1, W_\mu^2, W_\mu^3$, and B_μ :

$$\begin{aligned} W_\mu^\pm &= \frac{1}{\sqrt{2}}(W_\mu^1 \pm iW_\mu^2) \\ Z^\mu &= \frac{1}{\sqrt{(g^2 + g'^2)}}(-g'B_\mu + gW_\mu^3) \\ A^\mu &= \frac{1}{\sqrt{(g^2 + g'^2)}}(gB_\mu + g'W_\mu^3) \end{aligned} \tag{2.9}$$

²⁰⁵ And the masses of these fields are given by:

$$\begin{aligned} M_W^2 &= \frac{1}{4}g^2v^2 \\ M_Z^2 &= \frac{1}{4}(g^2 + g'^2)v^2 \\ M_A^2 &= 0 \end{aligned} \tag{2.10}$$

²⁰⁶ This produces exactly the particles we observe - three massive gauge bosons and a single
²⁰⁷ massless photon. The massless photon represents the portion of the gauge symmetry, a single
²⁰⁸ $U(1)$ of the electromagnetic force, that remains unbroken by the VEV.

²⁰⁹ Interactions with the Higgs field also lead to the generation of the fermion masses, which
²¹⁰ in the Lagrangian take the form:

$$-\lambda_\psi(\bar{\psi}_L\phi\psi_R + \bar{\psi}_R\phi^\dagger\psi_L) \tag{2.11}$$

211 After symmetry breaking has occurred and ϕ has taken on the value of the VEV as written
212 in equation 2.5, the mass terms for the fermions become $\lambda_\psi v$. Written this way, the fermion
213 masses are proportional to their Yukawa coupling to the VEV, λ_ψ .

214 Based on the equation 2.6, an additional mass term, $\mu^2 H^2$ arises from the potential $V(\Phi)$.
215 This term can be understood as an excitation of the Higgs field, a scalar boson with mass $M_H = \mu$.
216 This is the Higgs boson, which comes about as a natural prediction of electroweak symmetry
217 breaking.

218 The fermion's Yukawa coupling to the VEV take the same form as the fermion's coupling
219 to the Higgs boson - λ_ψ . Therefore, the strength of a fermion's interaction with the Higgs is
220 directly proportional to its mass. We now have a model that predicts a Higgs boson with mass
221 $M_H = \mu$, which interacts with the fermions with coupling strength λ_ψ . Because μ and λ_ψ are
222 free parameters of the theory, the mass of the Higgs boson and its interactions with the fermions
223 must be measured experimentally.

224 2.3 Limitations of the Standard Model

225 While the SM has great predictive power, there are still several experimental observations that the
226 SM fails to explain. For example, the SM predicts neutrinos to be massless, despite experimental
227 observation to the contrary.

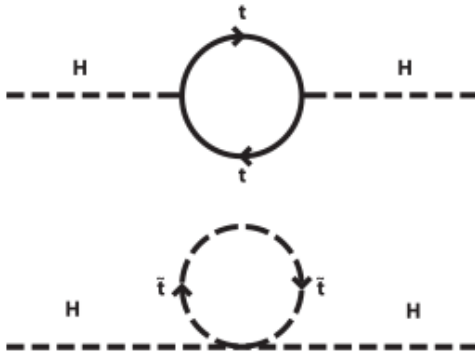


Figure 2.3: Above diagram is the leading order correction to the Higgs mass via a top quark loop, and below is the stop squark loop, coming from a supersymmetric extension of the SM, that provides a potential cancellation of the top diagram [6].

²²⁸ **3 Effective Field Theory in $t\bar{t}H$ Production**

²²⁹ Higher dimension operators are a common way to paramaterize the effects of physics at very
²³⁰ high energies into

²³¹ **3.1 Extensions to the Higgs Sector**

²³² **3.2 Six Dimensional Operators**

²³³ While the SM has been tested to great precision, particularly at the LHC, it is generally accepted
²³⁴ that it is only valid up to a certain energy scale. It is assumed that above a certain energy, at the
²³⁵ scale where something like a Grand Unified Theory (GUT) or quantum gravity become relevant,
²³⁶ the SM will not be applicable.

237 Part III

238 The LHC and the ATLAS Detector

239 4 The LHC

240 The Large Hadron Collider (LHC) is a particle accelerator consisting of a 27 km ring, designed
241 to collide protons at high energy. Located outside of Geneva, Switzerland and buried about 100
242 m underground, it consists of a ring of superconducting magnets which are used to accelerate
243 opposing beams of protons - or lead ions - which collide at the center of one of the various
244 detectors located around the LHC ring which record the result of these collisions. These
245 detectors include two general purpose detectors, ATLAS and CMS, which are designed to make
246 precision measurements of a broad range of physics phenomenon, and two more specialized
247 experiments, LHCb and ALICE, which are optimized to study b-quarks and heavy-ion physics,
248 respectively.

249 The LHC first began running in 2009 at a proton-proton center of mass energy of $\sqrt{s} = 8$
250 TeV. It operated at this energy from 2009 to 2012, known as Run 1, and data collected during
251 this period was used in discovering the Higgs Boson. The LHC began running again in 2015,
252 and collected data at an increased energy of $\sqrt{s} = 13$ TeV until 2018, a period referred to as Run
253 2.

254 The LHC consists of a chain of accelerators, which accelerate the protons to higher and

higher energies until they are injected into the main ring. This process is summarized in figure 4.1. Protons extracted from a tank of ionized hydrogen are fed into a linear accelerator, LINAC2, where they reach an energy of 50 MeV. From there, they enter a series of three separate circular accelerators, before being injected into the main accelerator ring at an energy of 450 GeV. Within the main ring protons are separated into two separate beams moving in opposite directions, and their energy is increased to their full collision energy. Radiofrequency cavities are used to accelerate these particles and sort them into bunches. From 2015-2018, these bunches consisted of around 100 billion protons each with an energy of 6.5 TeV per proton, which collided at a rate of 40 MHz, or every 25 ns.

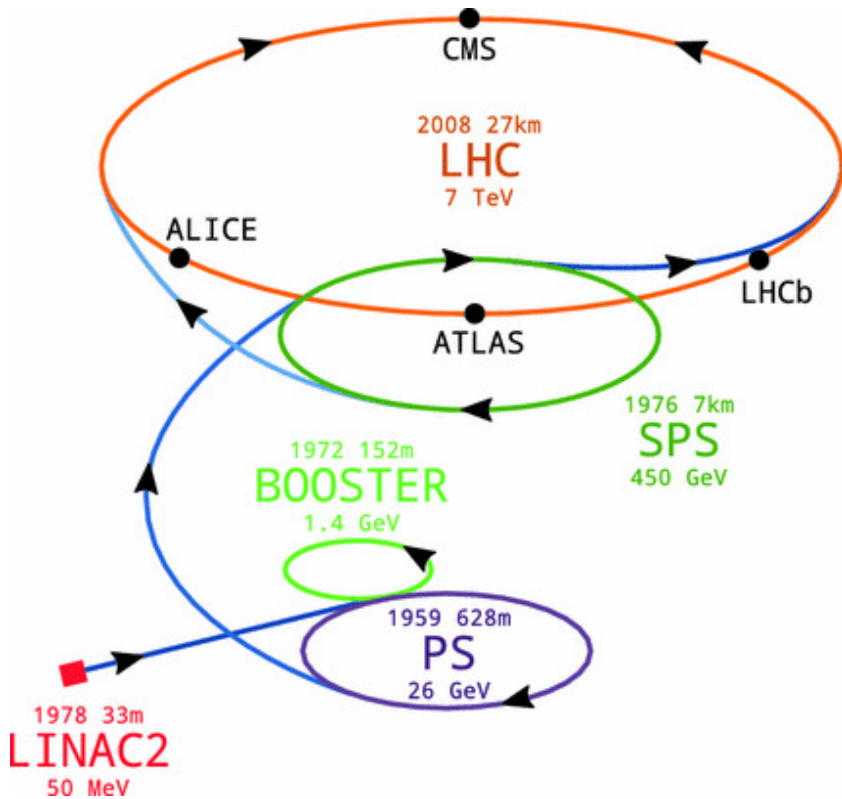


Figure 4.1: A summary of the accelerator chain used to feed protons into the LHC [].

264 Because these proton bunches consist of a large number of particles, each bunch crossing
 265 consists of not just one, but several direct proton-proton collisions. The number of interactions
 266 that occur per bunch crossing, μ , is known as pileup. During Run 2, the average pileup for bunch
 267 crossings was around $\langle \mu \rangle = 35$, with values typically ranging between 10 and 70.

268 The amount of data collected by the LHC is measured in terms of luminosity, which is the
 269 ratio of the number of events detected per unit time, $\frac{dN}{dt}$, and the interaction cross-section, σ .

$$\mathcal{L} = \frac{1}{\sigma} \frac{dN}{dt} \quad (4.1)$$

270 The design luminosity of the LHC is $10^{34} \text{ cm}^{-2} \text{ s}^{-1}$, however the LHC has achieved a
 271 luminosity of over $2 \times 10^{34} \text{ cm}^{-2} \text{ s}^{-1}$. The total luminosity is then this instantaneous luminosity
 272 integrated over time.

$$\mathcal{L}_{\text{int}} = \int \mathcal{L} dt \quad (4.2)$$

273 The integrated luminosity collected by the ATLAS detector as of the end of 2018 is around
 274 140 fb^{-1} , exceeding the expected integrated luminosity of 100 fb^{-1} .

275 5 The ATLAS Detector

276 ATLAS (a not terribly natural acronym for “A Toroidal LHC Apparatus”) is a general purpose
 277 detector designed to maximize the detection efficiency of all physics objects, including leptons,
 278 jets, and photons. This means it is capable of measuring all SM particles, with the exception of
 279 neutrinos, the presence of which can be inferred based on missing transverse momentum. The
 280 detector measures 44 m long, and 25 m tall.

281 The ATLAS detector consists of multiple layers, each of which serves a different purpose
 282 in reconstructing collisions. At the very center of the detector is the interaction point where the
 283 proton beams of the LHC collide.

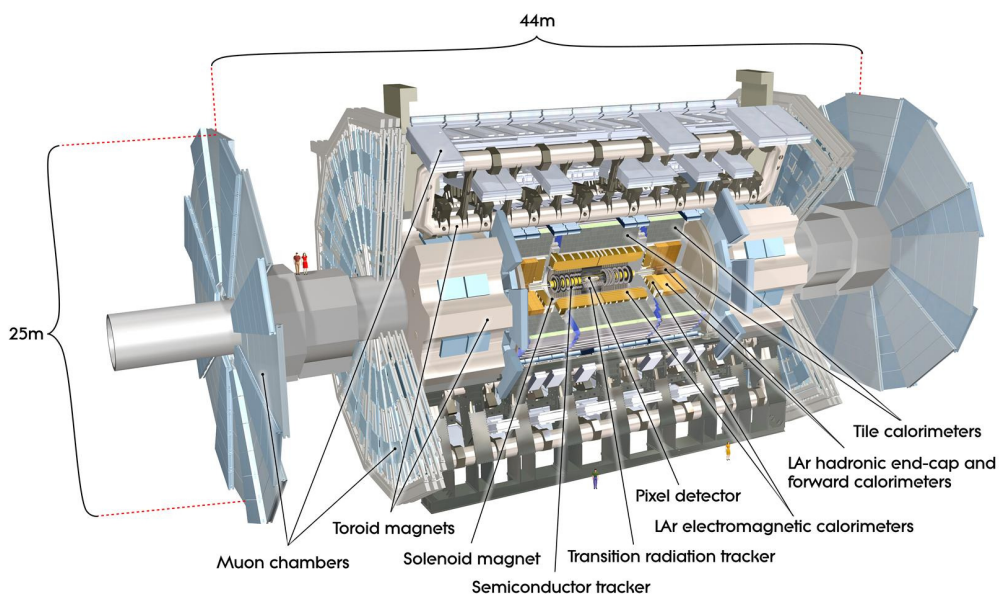


Figure 5.1: Cutaway view of the ATLAS detector, with labels of its major components [].

284 **5.1 Inner Detector**

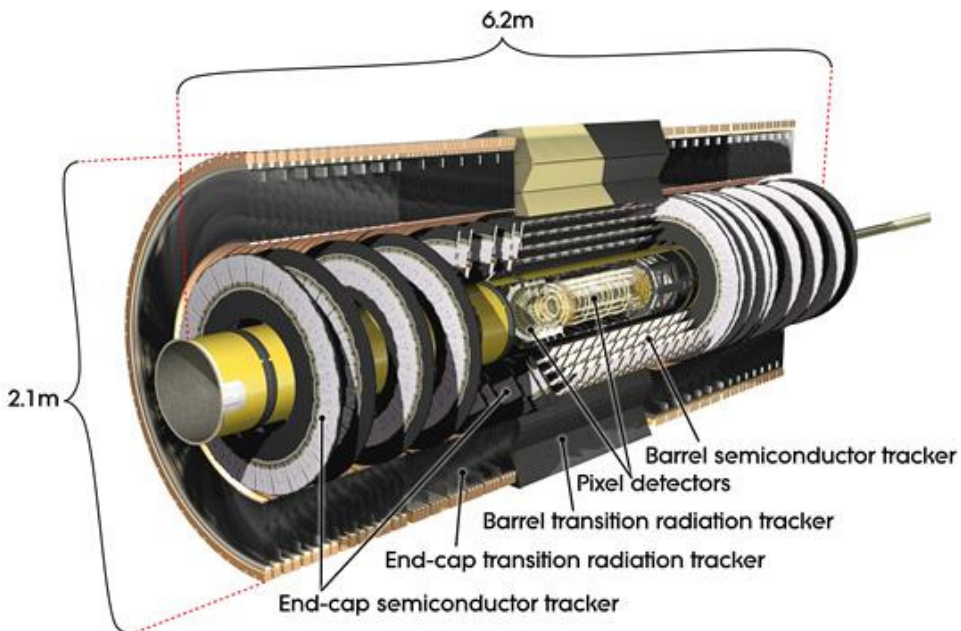


Figure 5.2: Cutaway view of the Inner Detector [].

285 Just surrounding the interaction point is the Inner Detector, designed to track the path
 286 of charged particles moving through the detector. An inner solenoid surrounding the Innder
 287 Detector is used to produces a magnetic field of 2 T. This large magnetic field causes the path
 288 of charged particles moving through the Inner Detector to bend. Because this magnetic field is
 289 uniform and well known, it can be used in conjunction with the curvature of a particles path to
 290 measure its charge and momentum.

291 The Inner Detector consists of three components - the Pixel Detector, the Semi-Conductor
 292 Tracker (SCT), and the Transition Radiation Tracker (TRT). The Pixel Detector is the innermost
 293 of these, beginning just 33.25 mm away from the beam line. It consists of three silicon layers

294 along the barrel, as well as three endcap layers, covering a range of $|\eta| < 2.5$.

295 The Semiconductor Tracker (SCT) is similar to the Pixel detector, but uses long strips
 296 rather than small pixel to cover a larger spatial area.

297 **5.2 Calorimeters**

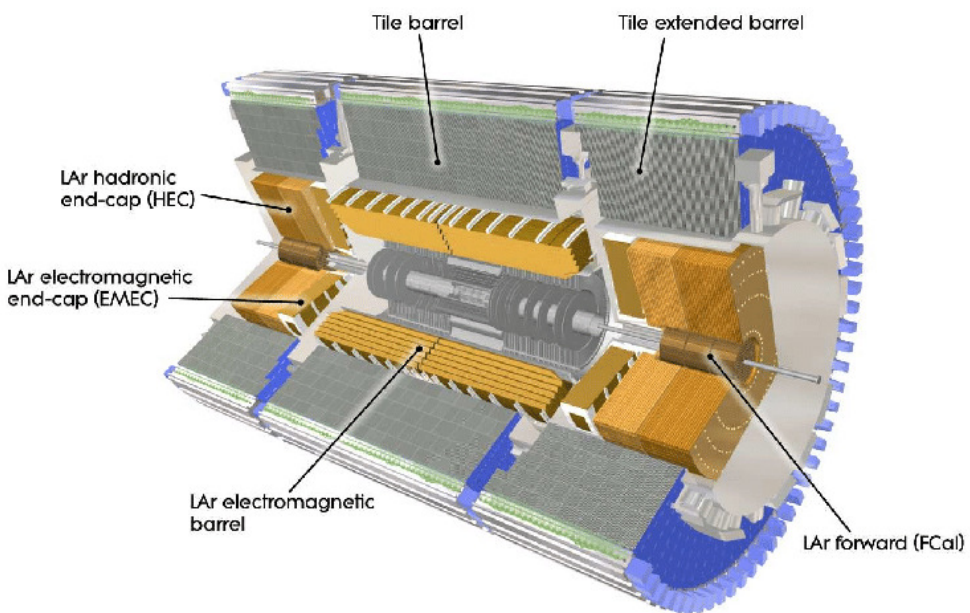


Figure 5.3: Cutaway view of the calorimeter system of the ATLAS detector [].

298 Situated outside the Inner Detector are two concentric calorimeters. The inner calorimeter
 299 uses liquid argon (LAr) to measure energy of particles that interact electromagnetically, which
 300 includes photons and any charged particle. The LAr calorimeter is made of heavy metals,
 301 primarily lead and copper, which causes electromagnetically interacting particles to shower,
 302 depositing their energy in the detector. The showering of the high energy particles that pass

303 through calorimeter cause the liquid argon to ionize, and the ionized electrons are detected by
304 electronic readouts. The LAr calorimeter consists of around 180,000 readout channels.

305 The outer calorimeter measures the energy from particles that pass through the EM calor-
306 imeter, and measures the energy of particles that interact via the strong force. This is primarily
307 hadrons. It is composed of steel plates to cause hadronic showering and scintillating tiles as the
308 active material. The signals from the hadronic calorimeter are read out by photomultiplier tubes
309 (PMTs).

310 **5.3 Muon Spectrometer**

311 Because muons are heavier than electrons and photons, and do not interact via the strong force,
312 they generally pass through the detector without being stopped by the calorimeters. The outermost
313 components of the detector are designed specifically to measure the energy and momentum of
314 muons produced in the LHC. The muon spectrometer consists of tracking and triggering system.
315 It extends from the outside of the calorimeter system, about a 4.25 m radius from the beam line,
316 to a radius of 11 m. This large detector system is necessary to accurately measure the momentum
317 of muons, which is essential not only for measurements involving the muons themselves, but also
318 to accurately estimate the missing energy in each event.

319 Two large toroidal magnets within the muon system generate a large magnetic field which
320 covers an area 26 m long with a radius of 10 m. Because the area covered by this magnet system
321 is so large, a uniform magnetic field like the one produced in the Inner Detector is impractical.

322 Instead, the magnetic field that exists in the muon spectrometer ranges between 2 T and 8 T, and
323 is much less uniform. The path of the muons passing through the spectrometer is bent by this
324 field, allowing their charge to be determined.

325 1200 tracking chambers are placed in the muon system in order to precisely measure the
326 tracks of muons with high spatial resolution.

327 **5.4 Trigger System**

328 Because of the high collision rate and large amount of data collected by the various subdetectors,
329 ATLAS produces far more data than can actually be stored. Each event produces around 25 Mb
330 of raw data, which multiplied by the bunch crossing rate of 40 MHz, comes out to around a
331 petabyte of data every second. The information from every event cannot practically be stored,
332 therefore a sophisticated trigger system is employed in real time to determine whether events are
333 sufficiently interesting to be worth storing.

334 The trigger system in ATLAS involves multiple levels, each of which select out which
335 events move on to the next level of scrutiny. The level-1 trigger uses hardware information from
336 the calorimeters and muon spectrometer to select events that contain candidates for particles
337 commonly used in analysis, such as energetic leptons and jets. The level-1 trigger reduces the
338 rate of events from 40 MHz to around 100 kHz.

339 Events that pass the level-1 trigger move to the High-Level Trigger (HLT). The HLT takes
 340 place outside of the detector in software, and looks for properties such as a large amount of
 341 missing transverse energy, well defined leptons, and multiple high energy jets. Events that pass
 342 the HLT are stored and used for analysis. Because the specifics of the HLT are determined by
 343 software rather than hardware, the thresholds can be changed throughout the run of the detector
 344 in response to run conditions such as changes to pileup and luminosity. After the HLT is applied,
 345 the event rate is reduced to around 1000 per second, which are recorded for analysis.

346 **Part IV**

347 **Search for Dimension-Six Operators**

348 **6 Data and Monte Carlo Samples**

349 For both data and Monte Carlo (MC) simulations, samples were prepared in the `xAOD` format,
 350 which was used to produce a `xAOD` based on the `HIGG8D1` derivation framework. This framework
 351 was designed for the main $t\bar{t}H$ multi-lepton analysis. Because this analysis targets events with
 352 multiple light leptons, as well as tau hadrons, this framework skims the dataset of any events that
 353 do not meet at least one of the following requirements:

- 354 • at least two light leptons within a range $|\eta| < 2.6$, with leading lepton $p_T > 15$ GeV and
 355 subleading lepton $p_T > 5$ GeV

- at least one light lepton with $p_T > 15 \text{ GeV}$ within a range $|\eta| < 2.6$, and at least two hadronic taus with $p_T > 15 \text{ GeV}$.

358 Samples were then generated from these HIGG8D1 derivations using a modified version of
359 AnalysisBase version 21.2.127.

360 6.1 Data Samples

361 The study uses proton-proton collision data collected by the ATLAS detector from 2015 through
362 2018, which represents an integrated luminosity of 139 fb^{-1} and an energy of $\sqrt{s} = 13 \text{ TeV}$. All
363 data used in this analysis was included in one the following Good Run Lists:

- data15_13TeV.periodAllYear_DetStatus-v79-repro20-02_DQDefects-00-02-02
_PHYS_StandardGRL_All_Good_25ns.xml
 - data16_13TeV.periodAllYear_DetStatus-v88-pro20-21_DQDefects-00-02-04
_PHYS_StandardGRL_All_Good_25ns.xml
 - data17_13TeV.periodAllYear_DetStatus-v97-pro21-13_Unknown_PHYS_StandardGRL
_All_Good_25ns_Triggerno17e33prim.xml
 - data18_13TeV.periodAllYear_DetStatus-v102-pro22-04_Unknown_PHYS_StandardGRL
_All_Good_25ns_Triggerno17e33prim.xml

³⁷² **6.2 Monte Carlo Samples**

³⁷³ Several Monte Carlo (MC) generators were used to simulate both signal and background pro-
³⁷⁴ cesses. For all of these, the effects of the ATLAS detector are simulated in Geant4. The specific
³⁷⁵ event generator used for each of these MC samples is listed in table 1.

Table 1: The configurations used for event generation of signal and background processes, including the event generator, matrix element (ME) order, parton shower algorithm, and parton distribution function (PDF).

Process	Event generator	ME order	Parton Shower	PDF
ttH	MG5_AMC (MG5_AMC)	NLO (NLO)	PYTHIA 8 (HERWIG++)	NNPDF 3.0 NLO [Ball:2014uwa] (CT10 [ct10])
t̄W	MG5_AMC (SHERPA 2.1.1)	NLO (LO multileg)	PYTHIA 8 (SHERPA)	NNPDF 3.0 NLO (NNPDF 3.0 NLO)
t̄t(Z/γ* → ll)	MG5_AMC	NLO	PYTHIA 8	NNPDF 3.0 NLO
VV	SHERPA 2.2.2	MEPS NLO	SHERPA	CT10
t̄t	POWHEG-BOX v2 [powhegtt]	NLO	PYTHIA 8	NNPDF 3.0 NLO
t̄tγ	MG5_AMC	LO	PYTHIA 8	NNPDF 2.3 LO
tZ	MG5_AMC	LO	PYTHIA 6	CTEQ6L1
tHqb	MG5_AMC	LO	PYTHIA 8	CT10
tHW	MG5_AMC (SHERPA 2.1.1)	NLO (LO multileg)	HERWIG++ (SHERPA)	CT10 (NNPDF 3.0 NLO)
tWZ	MG5_AMC	NLO	PYTHIA 8	NNPDF 2.3 LO
t̄t̄t, t̄t̄t̄t	MG5_AMC	LO	PYTHIA 8	NNPDF 2.3 LO
t̄tW+W-	MG5_AMC	LO	PYTHIA 8	NNPDF 2.3 LO
s-, t-channel, Wt single top	POWHEG-BOX v1 [powhegstp]	NLO	PYTHIA 6	CT10
qqVV, VVV				
Z → l+l-	SHERPA 2.2.1	MEPS NLO	SHERPA	NNPDF 3.0 NLO

³⁷⁶ **7 Object Reconstruction**

³⁷⁷ All analysis channels considered in this note share a common object selection for leptons and
³⁷⁸ jets, as well as a shared trigger selection.

³⁷⁹ **7.1 Trigger Requirements**

³⁸⁰ Events are required to be selected by dilepton triggers, as summarized in table 2.

Dilepton triggers (2015)	
$\mu\mu$ (asymm.)	HLT_mu18_mu8noL1
ee (symm.)	HLT_2e12_lhloose_L12EM10VH
$e\mu, \mu e$ (\sim symm.)	HLT_e17_lhloose_mu14
Dilepton triggers (2016)	
$\mu\mu$ (asymm.)	HLT_mu22_mu8noL1
ee (symm.)	HLT_2e17_lhvloose_nod0
$e\mu, \mu e$ (\sim symm.)	HLT_e17_lhloose_nod0_mu14
Dilepton triggers (2017)	
$\mu\mu$ (asymm.)	HLT_mu22_mu8noL1
ee (symm.)	HLT_2e24_lhvloose_nod0
$e\mu, \mu e$ (\sim symm.)	HLT_e17_lhloose_nod0_mu14
Dilepton triggers (2018)	
$\mu\mu$ (asymm.)	HLT_mu22_mu8noL1
ee (symm.)	HLT_2e24_lhvloose_nod0
$e\mu, \mu e$ (\sim symm.)	HLT_e17_lhloose_nod0_mu14

Table 2: List of lowest p_T -threshold, un-prescaled dilepton triggers used for 2015-2018 data taking.

³⁸¹ **7.2 Light Leptons**

³⁸² Electron candidates are reconstructed from energy clusters in the electromagnetic calorimeter that
³⁸³ are associated with charged particle tracks reconstructed in the inner detector [**ATLAS-CONF-2016-024**].
³⁸⁴ Electron candidates are required to have $p_T > 10$ GeV and $|\eta_{\text{cluster}}| < 2.47$. Candidates in the
³⁸⁵ transition region between different electromagnetic calorimeter components, $1.37 < |\eta_{\text{cluster}}| <$
³⁸⁶ 1.52, are rejected. A multivariate likelihood discriminant combining shower shape and track

387 information is used to distinguish prompt electrons from nonprompt leptons, such as those
 388 originating from hadronic showers.

389 To further reduce the non-prompt contribution, the track of each electron is required to
 390 originate from the primary vertex; requirements are imposed on the transverse impact parameter
 391 significance ($|d_0|/\sigma_{d_0}$) and the longitudinal impact parameter ($|\Delta z_0 \sin \theta_\ell|$), as shown in table
 392 ??.

393 Muon candidates are reconstructed by combining inner detector tracks with track segments
 394 or full tracks in the muon spectrometer [**PERF-2014-05**]. Muon candidates are required to have
 395 $p_T > 10$ GeV and $|\eta| < 2.5$. All leptons are required to be isolated, and pass a non-prompt BDT
 396 selection described in detail in [**ttH_paper**].

397 7.3 Jets

398 Jets are reconstructed from calibrated topological clusters built from energy deposits in the
 399 calorimeters [**ATL-PHYS-PUB-2015-015**], using the anti- k_t algorithm with a radius parameter
 400 $R = 0.4$. Jets with energy contributions likely arising from noise or detector effects are removed
 401 from consideration [**ATLAS-CONF-2015-029**], and only jets satisfying $p_T > 25$ GeV and
 402 $|\eta| < 2.5$ are used in this analysis. For jets with $p_T < 60$ GeV and $|\eta| < 2.4$, a jet-track
 403 association algorithm is used to confirm that the jet originates from the selected primary vertex,
 404 in order to reject jets arising from pileup collisions [**PERF-2014-03**].

405 **7.4 Missing Transverse Energy**

406 Because all $t\bar{t}H - ML$ channels considered include multiple neutrinos, missing transverse
 407 energy (E_T^{miss}) is present in each event. The missing transverse momentum vector is defined as
 408 the inverse of the sum of the transverse momenta of all reconstructed physics objects as well
 409 as remaining unclustered energy, the latter of which is estimated from low- p_T tracks associated
 410 with the primary vertex but not assigned to a hard object [ATL-PHYS-PUB-2015-027].

411 **8 Higgs Momentum Reconstruction**

412 Reconstructing the momentum of the Higgs boson is a particular challenge for channels with
 413 leptons in the final state: Because all channels include at least two neutrinos in the final state, the
 414 Higgs can never be fully reconstructed. However, the momentum spectrum can be well predicted
 415 by a neural network when provided with the four-vectors of the Higgs Boson decay products, as
 416 shown in section 8.1. With this in mind, several layers of MVAs are used to reconstruction the
 417 Higgs momentum.

418 The first layer is a model designed to select which jets are most likely to be the b-jets
 419 that came from the top decay, detailed in section 8.2. As described in section 8.3, the kinematics
 420 of these jets are fed into the second layer, which is designed to identify the decay products of
 421 the Higgs Boson itself. The kinematics of these particles are then fed into yet another neural-

422 network, which predicts the momentum of the Higgs (8.4). MVAs are also used in the analysis
423 to determine the decay of the Higgs boson in the 3l channel (8.5).

424 For all of these models, the Keras neural network framework, with Tensorflow as the
425 backend, is used, and the number of hidden layers and nodes are determined using grid search
426 optimization. Each neural network uses the LeakyReLU activation function, a learning rate
427 of 0.01, and the Adam optimization algorithm, as alternatives are found to either decrease or
428 have no impact on performance. Batch normalization is applied after each layer. For the
429 classification algorithms (b-jet matching, Higgs reconstruction, and 3l decay identification)
430 binary-cross entropy is used as the loss function, while the p_T reconstruction algorithm uses
431 MSE.

432 The specific inputs features used for each model are arrived at through a process of trial
433 and error - features considered potentially useful are tried, and those that are found to increase
434 performance are included. While each model includes a relatively large number of features,
435 some using upwards of 30, this inclusive approach is found to maximize the performance of each
436 model while decreasing the variance compared to a reduced number of inputs. Each input feature
437 is validated by comparing MC simulations to 80 fb^{-1} of data, as shown in the sections below.

438 8.1 Decay Candidate Reconstruction

439 Machine Learning algorithms are trained to identify the decay products of the Higgs Boson
440 using MC simulations of $t\bar{t}H$ events. These include light leptons and jets. Reconstructed

441 physics objects are matched to truth level particles, in order to identify the parents of these
442 reconstructed objects. The kinematics of the decay product candidates as well as event level
443 variables are used as inputs.

444 Leptons considered as possible Higgs and top decay candidates are required to pass the
445 selection described in section 7.2. For jets, however, it is found that a large fraction that originate
446 from either the top decay or the Higgs decay fall outside the selection described in section 7.3.
447 Specifically, jets from the Higgs decay tend to be soft, with 32% having $p_T < 25$ GeV. Therefore
448 jets with $p_T < 15$ GeV are considered as possible candidates in the models described below. By
449 contrast, less than 5% of the jets originating from the Higgs fall below this p_T . The jets are found
450 to be well modeled even down to this low p_T threshold, as shown in section 9.1. The impact of
451 using different p_T selection for the jet candidates is considered in detail in section ???. As they
452 are expected to originate from the primary vertex, jets are also required to pass a JVT cut.

453 8.2 b-jet Identification

454 Including the kinematics of the b-jets that originate from the top decay is found to improve the
455 identification of the Higgs decay products, and improve the accuracy with which the Higgs
456 momentum can be reconstructed. Because these b-jets are reconstructed by the detector with
457 high efficiency (just over 90% of the time), and can be identified relatively consistently, the first
458 step in reconstructing the Higgs is selecting the b-jets from the top decay.

459 Exactly two b-jets are expected in the final state of $t\bar{t}H - ML$ events. However, in both
 460 the 3l and 2lSS channels, only one or more b-tagged jets are required (where the 70% DL1r b-tag
 461 working point is used). Therefore, for events which have exactly one, or more than two, b-tagged
 462 jets, deciding which combination of jets correspond to the top decay is non-trivial. Further,
 463 events with 1 b-tagged jet represent just over half of all $t\bar{t}H - ML$ events. Of those, both b-jets
 464 are reconstructed by the detector 75% of the time. Therefore, rather than adjusting the selection
 465 to require exactly 2 b-tagged jets, and losing more than half of the signal events, a neural network
 466 is used to predict which pair of jets is most likely to correspond to truth b-jets.

467 Once the network is trained, all possible pairings of jets are fed into the model, and the pair
 468 of jets with the highest output score are taken to be b-jets in successive steps of the analysis.

469 8.2.1 2lSS Channel

470 For the 2lSS channel, the input features shown in table 3 are used for training. Here j_0 and j_1
 471 are the two jet candidates, while l_0 and l_1 are the two leptons in the event, ordered by p_T . jet
 472 DL1r is an integer corresponding to the calibrated b-tagging working points reached by each jet,
 473 where 5 represents the tightest working point and 1 represents the loosest. The variables nJets
 474 DL1r 60% and nJets DL1r 85% represent the number of jets in the event passing the 60% and
 475 85% b-tag working points, respectively.

476 As there are far more incorrect combinations than correct ones, by a factor of more than
 477 20:1, the training set is resampled to reduce the fraction of incorrect combinations. A random

jet p_T 0	jet p_T 1	Lepton p_T 0
Lepton p_T 1	jet η 0	jet η 1
$\Delta R(j_0)(j_1)$	$M(j_0 j_1)$	$\Delta R(l_0)(j_0)$
$\Delta R(l_0)(j_1)$	$\Delta R(l_1)(j_0)$	$\Delta R(l_1)(j_1)$
$M(l_0 j_0)$	$M(l_0 j_1)$	$M(l_1 j_0)$
$M(l_1 j_1)$	jet DL1r 0	jet DL1r 1
nJets OR DL1r 85	nJets OR DL1r 60	$\Delta R(j_0 l_0)(j_1 l_1)$
$\Delta R(j_0 l_1)(j_1 l_0)$	$p_T(j_0 j_1 l_0 l_1 E_T^{\text{miss}})$	$M(j_0 j_1 l_0 l_1 E_T^{\text{miss}})$
$\Delta\phi(j_0)(E_T^{\text{miss}})$	$\Delta\phi(j_1)(E_T^{\text{miss}})$	HT jets
nJets	E_T^{miss}	

Table 3: Input features used in the 2ISS b-jet identification algorithm

478 sample of 5 million incorrect entries are used for training, along with close 1 million correct
 479 entries. 10% of the dataset is set aside for testing, leaving around 5 million datapoints for
 480 training.

481 The difference between the distributions for a few of these features for the correct(i.e.
 482 both jets are truth b-jets), and incorrect combinations are shown in figure 8.1. The correct and
 483 incorrect contributions are scaled to the same integral, so as to better demonstrate the differences
 484 in the distributions.

485 The modeling of these inputs is validated against data, with figure 8.2 showing good
 486 general agreement between data and MC. Plots for the complete list of features can found in
 487 section A.

488 Based on the results of grid search evaluation, the optimal architecture is found to include
 489 5 hidden layers with 40 nodes each. No regularizer or dropout is added to the network, as
 490 overfitting is found to not be an issue. The output score distribution as well as the ROC curve for

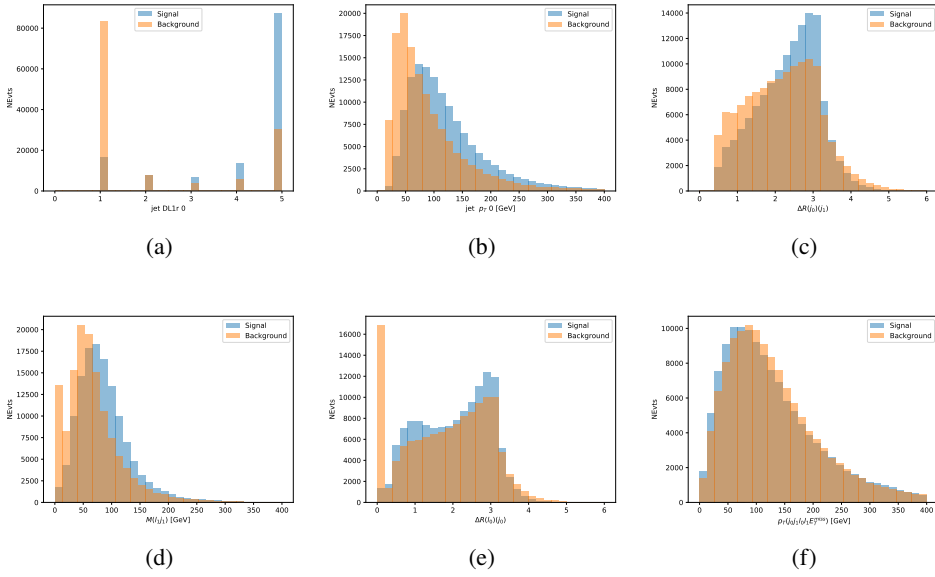


Figure 8.1: Input features for top2lSS training. The signal in blue represents events where both jet candidates are truth b-jets from top decays, and the orange is all other combinations. Scaled to the same number of events.

491 the trained model are shown in figure 8.2.1. The model is found to identify the correct pairing
492 of jets for 73% of 2lSS signal events on test data.

493 For point of comparison, a naïve approach to identify b-jets is used as well: The two jets
494 which pass the highest DL1r b-tag working point are assumed to be the b-jets from the top decay.
495 In the case that multiple jets meet the same b-tag working point, the jet with higher p_T is used.
496 This method identifies the correct jet pair 65% of the time.

497 The accuracy of the model for different values of n-bjets, compared to this naive approach,
498 is shown in table 4.

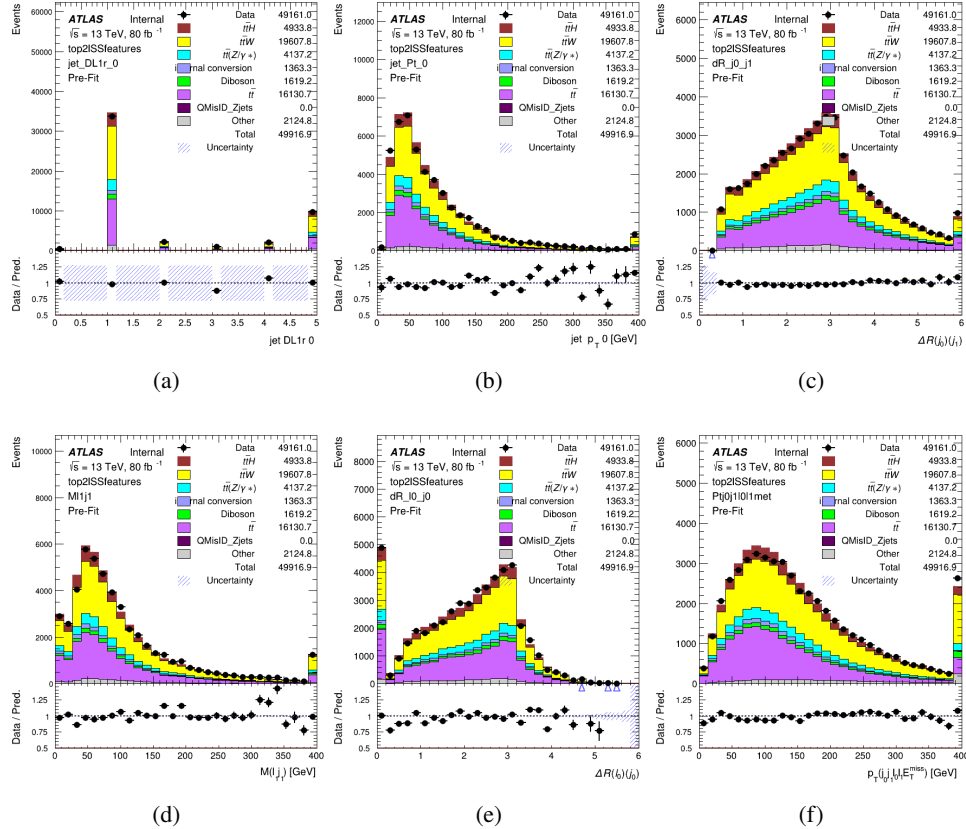


Figure 8.2: Data/MC comparisons of input features for top2ISS training for 80 fb^{-1} of data.

Table 4: Accuracy of the NN in identifying b-jets from tops in 2ISS events for, compared to the accuracy of taking the two highest b-tagged jets.

b-jet Selection	Neural Network	Naive
1 b-jet	58.6%	42.1%
2 b-jets	88.4%	87.1%
≥ 3 b-jets	61.7%	53.3%
Overall	73.9% %	67.2%

499 8.2.2 3l Channel

500 The input features used in the 3l channel are listed in table 5, with the same naming convention
501 as the 2ISS channel.

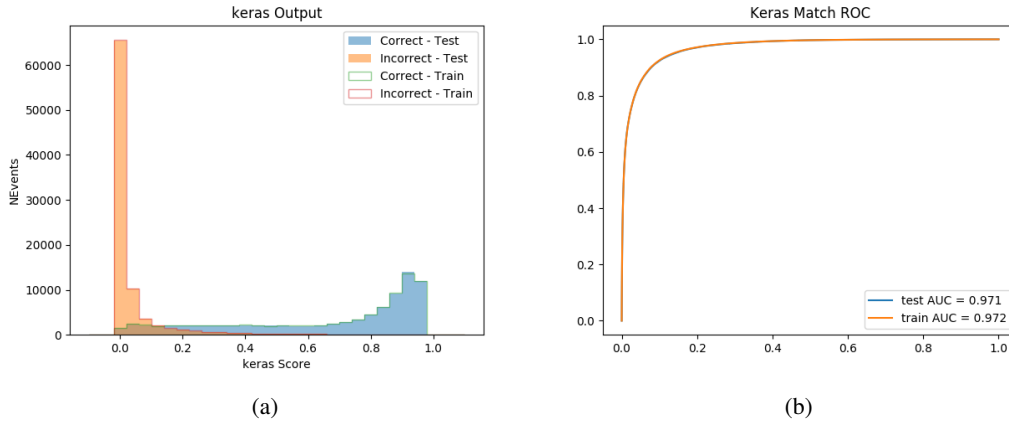


Figure 8.3: (a) the output score of the NN for correct and incorrect combinations of jets. (b) the ROC curve of the output, showing background rejection as a function of signal efficiency

jet p_T 0	jet p_T 1	jet η 0
jet η 1	Lepton p_T 0	Lepton p_T 1
Lepton p_T 2	$\Delta R(j_0)(j_1)$	$M(j_0 j_1)$
$\Delta R(l_0)(j_0)$	$\Delta R(l_1)(j_0)$	$\Delta R(l_2)(j_0)$
$\Delta R(l_0)(j_1)$	$\Delta R(l_1)(j_1)$	$\Delta R(l_2)(j_1)$
$M(l_0 j_0)$	$M(l_1 j_0)$	$M(l_2 j_0)$
$M(l_0 j_1)$	$M(l_1 j_1)$	$M(l_2 j_1)$
$\Delta R(j_0 l_0)(j_1 l_1)$	$\Delta R(j_0 l_0)(j_1 l_2)$	$\Delta R(j_0 l_1)(j_1 l_0)$
$\Delta R(j_0 l_2)(j_1 l_0)$	jet DL1r 0	jet DL1r 1
$p_T(j_0 j_1 l_0 l_1 l_2 E_T^{\text{miss}})$	$M(t j_0 j_1 l_0 l_1 l_2 E_T^{\text{miss}})$	$\Delta\phi(j_0)(E_T^{\text{miss}})$
$\Delta\phi(j_1)(E_T^{\text{miss}})$	HT Lepton	HT jets
nJets	E_T^{miss}	nJets OR DL1r 85
nJets OR DL1r 60		

Table 5: Input features

502 A few of these features are shown in figure 8.4, comparing the distributions for correct and
 503 incorrect combinations of jets.

504 The modeling of these inputs is validated against data, with figure 8.5 showing good
 505 general agreement between data and MC. Plots for the complete list of features can be found in
 506 section A.

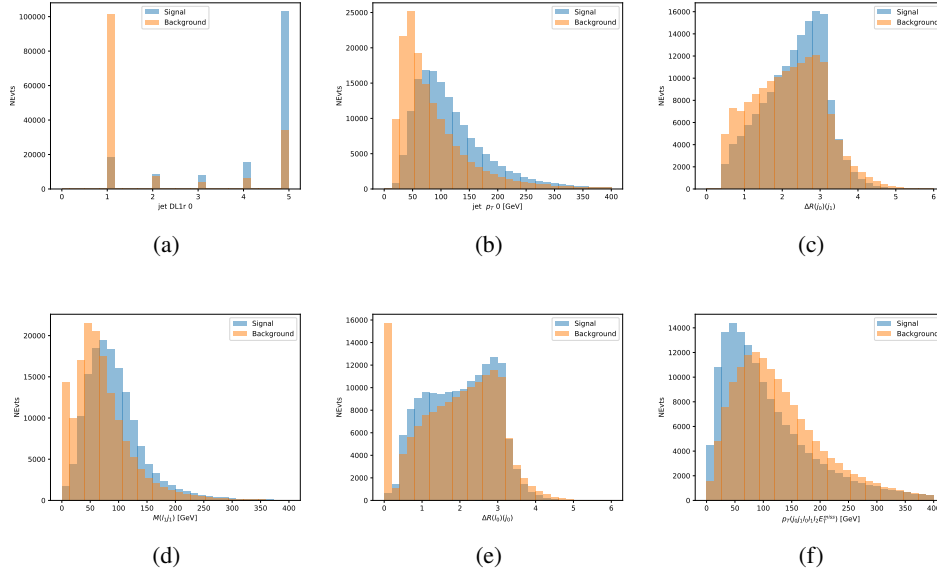


Figure 8.4: Input features for top3l training. The signal in blue represents events where both jet candidates are truth b-jets from top decays, and the orange is all other combinations. Scaled to the same number of events.

507 Again, the dataset is downsized to reduce the ratio of correct and incorrect combination
508 from 20:1, to 5:1. Around 7 million events are used for training, with 10% set aside for testing.
509 Based on the results of grid search evaluation, the optimal architecture is found to include 5
510 hidden layers with 60 nodes each. The output score distribution as well as the ROC curve for the
511 trained model are shown in figure 8.2.2.

512 This procedure is found to identify the correct pairing of jets for nearly 80% of 3l signal
513 events. The accuracy of the model is summarized in table 6.

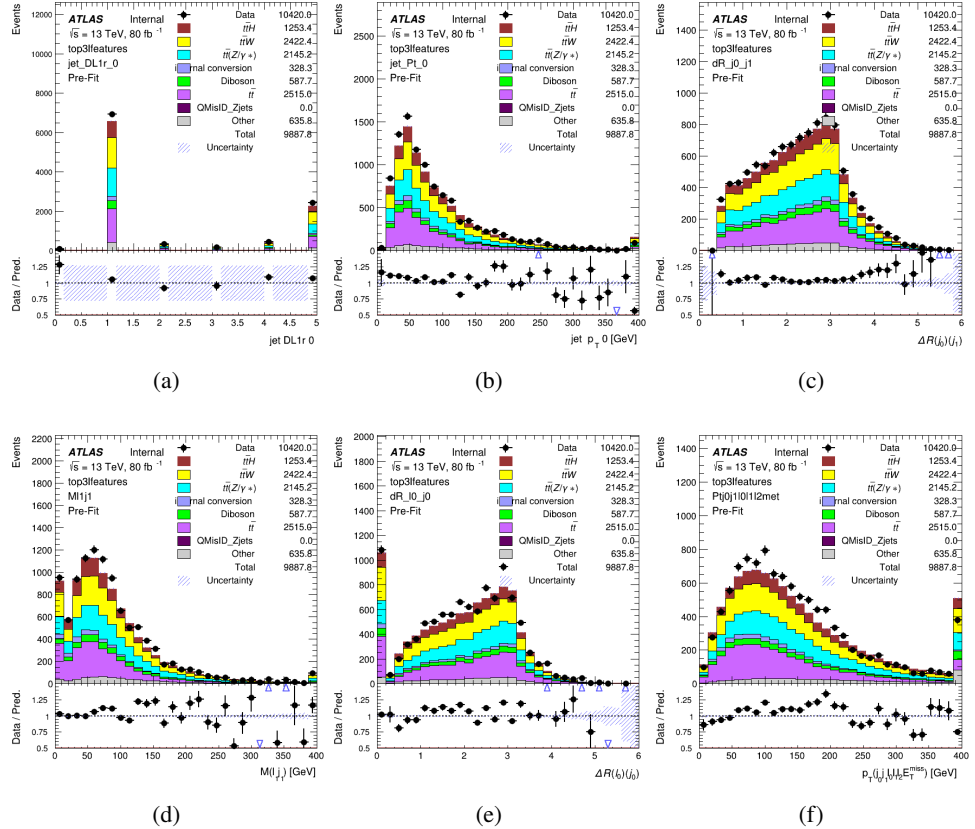
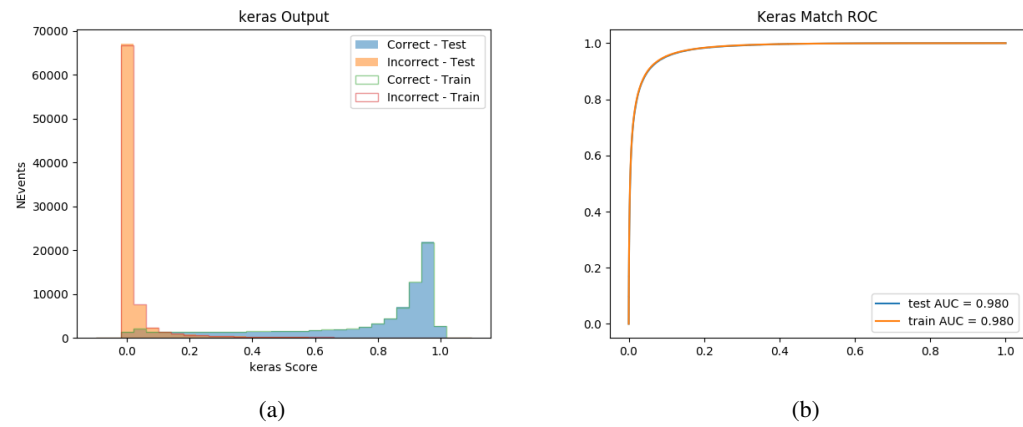
Figure 8.5: Data/MC comparisons of input features for top3l training for 80 fb^{-1} of data.

Figure 8.6: tmp

Table 6: Accuracy of the NN in identifying b-jets from tops, compared to the naive method of taking the highest b-tagged jets.

	NN	Naive
1 b-jet	69.0%	48.9%
2 b-jets	89.6%	88.3%
≥ 3 b-jets	55.7%	52.3%
Overall	79.8%	70.2%

514 8.3 Higgs Reconstruction

515 Techniques similar to the b-jet identification algorithms are employed to select the decay products
 516 of the Higgs: kinematics of all possible combinations of reconstructed objects are fed into a neural
 517 network to determine which of those is most mostly to be the decay products of the Higgs.

518 Again separate models are used for the 2lSS and 3l channels, while the 3l channel has now
 519 been split into two: $t\bar{t}H$ events with three leptons in the final state include both instances where
 520 the Higgs decays into a lepton (and a neutrino) and a pair of jets, and instances where the Higgs
 521 decays to two leptons.

522 3l events are therefore categorized as either semi-leptonic or fully-leptonic. In the semi-
 523 leptonic case the reconstructed decay products consist of two jets and a single leptons. For
 524 the fully-leptonic case, the decay products include 2 of the three leptons associated with the
 525 event. For training the models, events are separated into these two categories using truth level
 526 information. A separate MVA, described in section 8.5, is used to make this distinction at reco
 527 level and determine which model to use.

528 For all channels, the models described in section 8.2 are used to identify b-jet candidates,

529 whose kinematics are used to identify the Higgs decay products. These jets are not considered
530 as possible candidates for the Higgs decay, justified by the fact that these models are found to
531 misidentify jets from the Higgs decay as jets from the top decay less than 1% of the time.

532 **8.3.1 2ISS Channel**

533 For the 2ISS channel, the Higgs decay products include one light lepton and two jets. The neural
534 network is trained on the kinematics of different combinations of leptons and jets, as well as the
535 b-jets identified in section 8.2, with the specific input features listed in table ??.

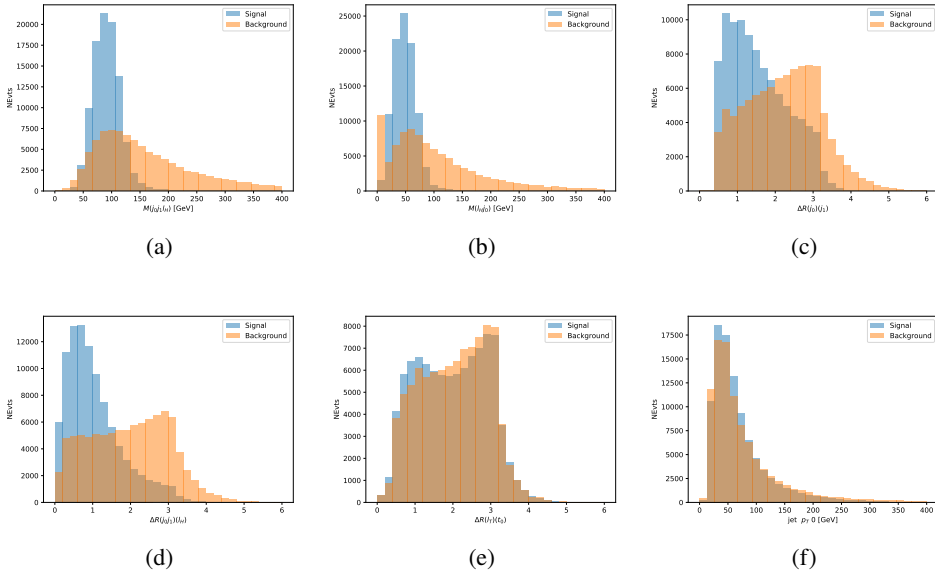


Figure 8.7: Input features for higgs2lSS training. The signal in blue represents events where both jet candidates are truth b-jets from top decays, and the orange is all other combinations. Scaled to the same number of events.

536 The modeling of these inputs is validated against data, with figure 8.2 showing good
 537 general agreement between data and MC. Plots for the complete list of features can found in
 538 section A.

539 The neural network identifies the correct combination 55% of the time. It identifies the
 540 correct lepton 85% of the time, and selects the correct lepton and at least one of the correct jets
 541 81% of the time.

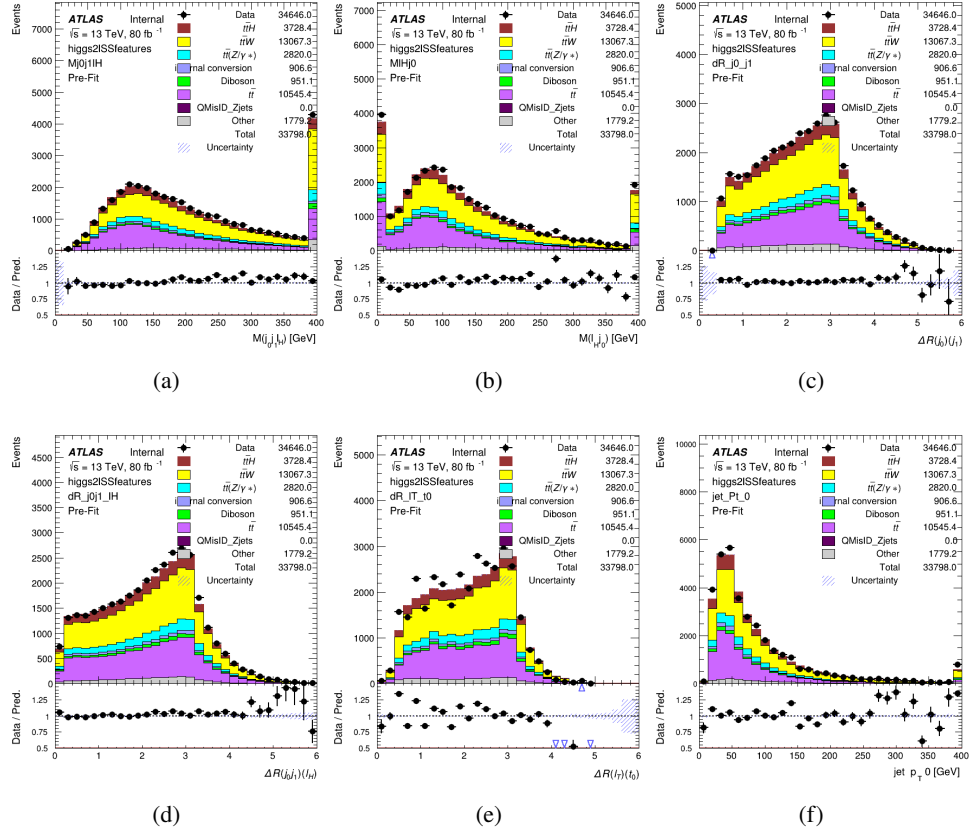


Figure 8.8: Data/MC comparisons of input features for higgs2lSS training for 80 fb^{-1} of data.

542 8.3.2 3l Semi-leptonic Channel

543 For 3l $t\bar{t}H$ where the Higgs decay semi-leptonically, the decay products include one of the three
 544 leptons and two jets. In this case, the other two leptons originated from the decay of the tops,
 545 meaning the opposite-sign (OS) lepton cannot have come the Higgs. This leave only the two
 546 same-sign (SS) leptons as possible Higgs decay products.

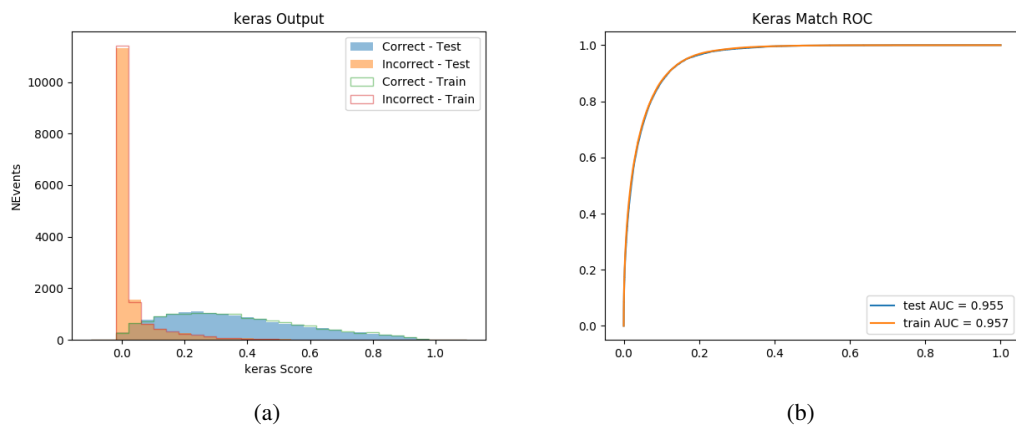


Figure 8.9: (a) the output score of the NN for correct and incorrect combinations of jets. (a) the ROC curve of the output, showing background rejection as a function of signal efficiency

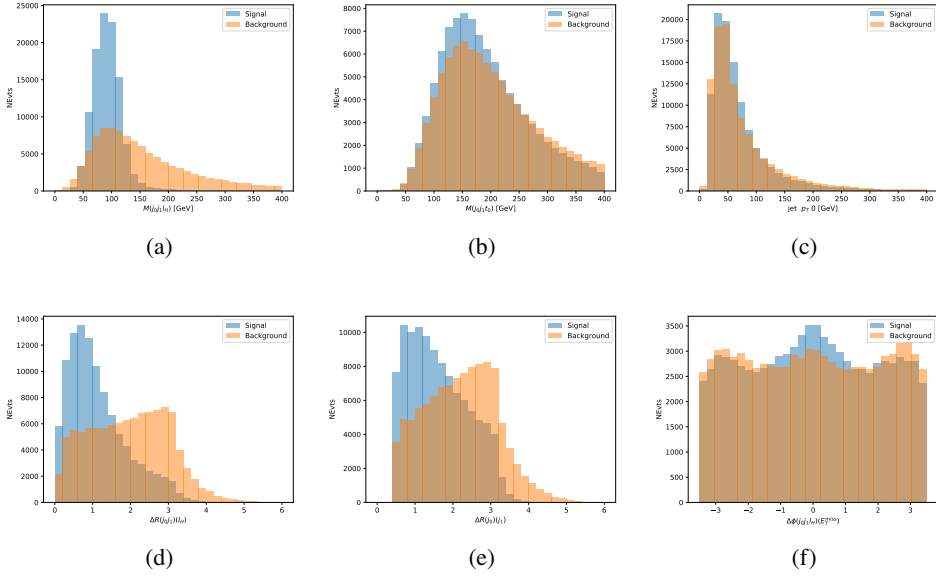


Figure 8.10: Input features for higgs3lS training. The signal in blue represents events where both jet candidates are truth b-jets from top decays, and the orange is all other combinations. Scaled to the same number of events.

547 The modeling of these inputs is validated against data, with figure 8.11 showing good
 548 general agreement between data and MC. Plots for the complete list of features can found in
 549 section A.

550 The neural network identifies the correct combination 65% of the time. It identifies the
 551 correct lepton 85% of the time, anselects the correct lepton and at least one of the correct jets
 552 83% of the time.

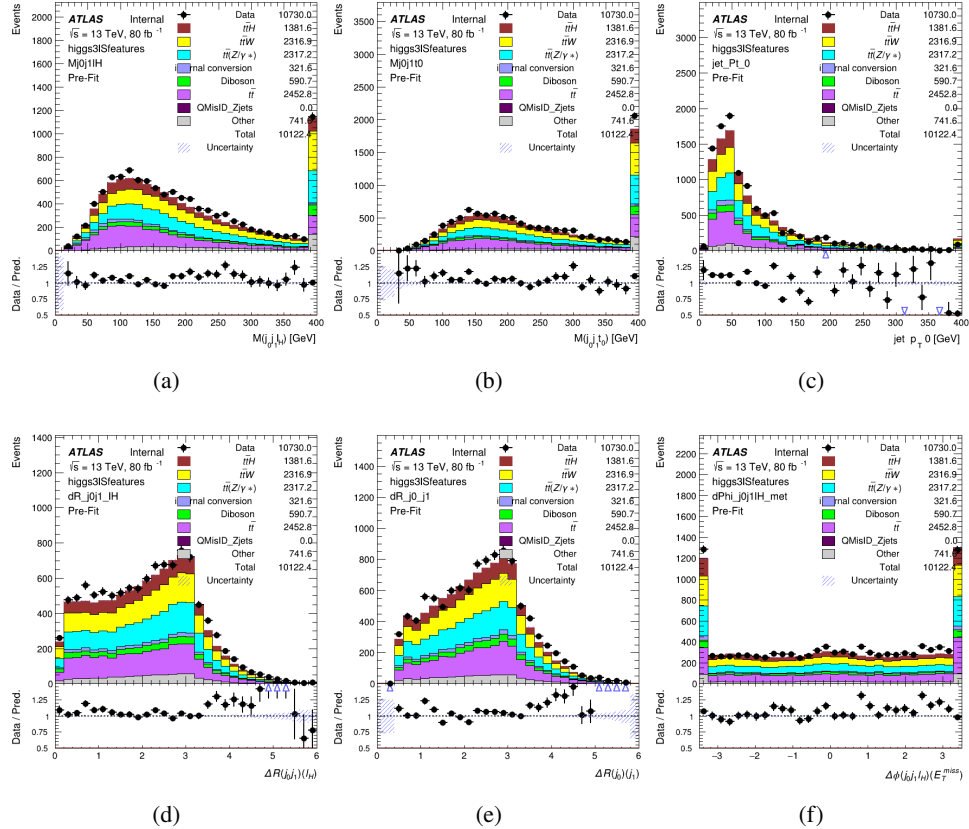


Figure 8.11: Data/MC comparisons of input features for higgs3lS training for 80 fb^{-1} of data.

553 8.3.3 3l Fully-leptonic Channel

554 In the fully-leptonic 3l case, the goal is identify which two of the three leptons originated from
 555 the Higgs decay. Since one of these two must be the OS lepton, this problem is reduced to
 556 determining which of the two SS leptons originated from the Higgs. The kinematics of both
 557 possibilities are used for training, one where the SS lepton from the Higgs is correctly labeled,
 558 and one where it is not.

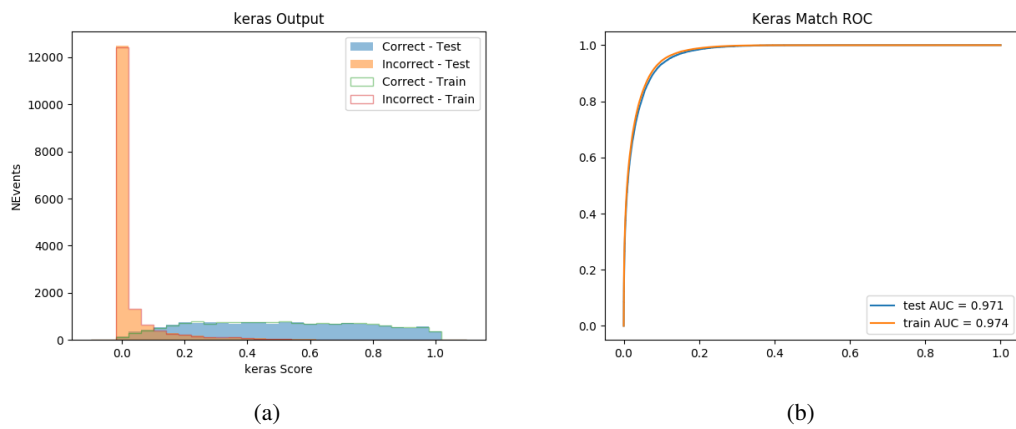


Figure 8.12: (a) the output score of the NN for correct and incorrect combinations of jets. (a) the ROC curve of the output, showing background rejection as a function of signal efficiency

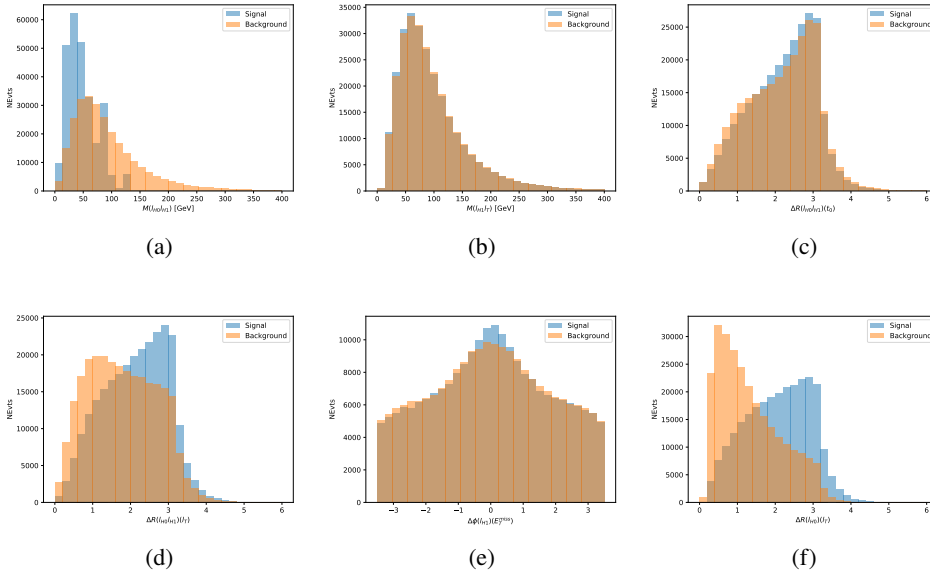


Figure 8.13: Input features for higgs3lF training. The signal in blue represents events where both jet candidates are truth b-jets from top decays, and the orange is all other combinations. Scaled to the same number of events.

559 The modeling of these inputs is validated against data, with figure 8.14 showing good
 560 general agreement between data and MC. Plots for the complete list of features can found in
 561 section A.

562 The correct lepton is identified 80% of the time.

563 8.4 p_T Prediction

564 Once the most probable decay products have been identified, their kinematics are used as inputs
 565 to a regression model which attempts to predict the momentum of the Higgs Boson. Once again,
 566 a DNN is used. Input variables representing the b-jets and leptons not from the Higgs decay

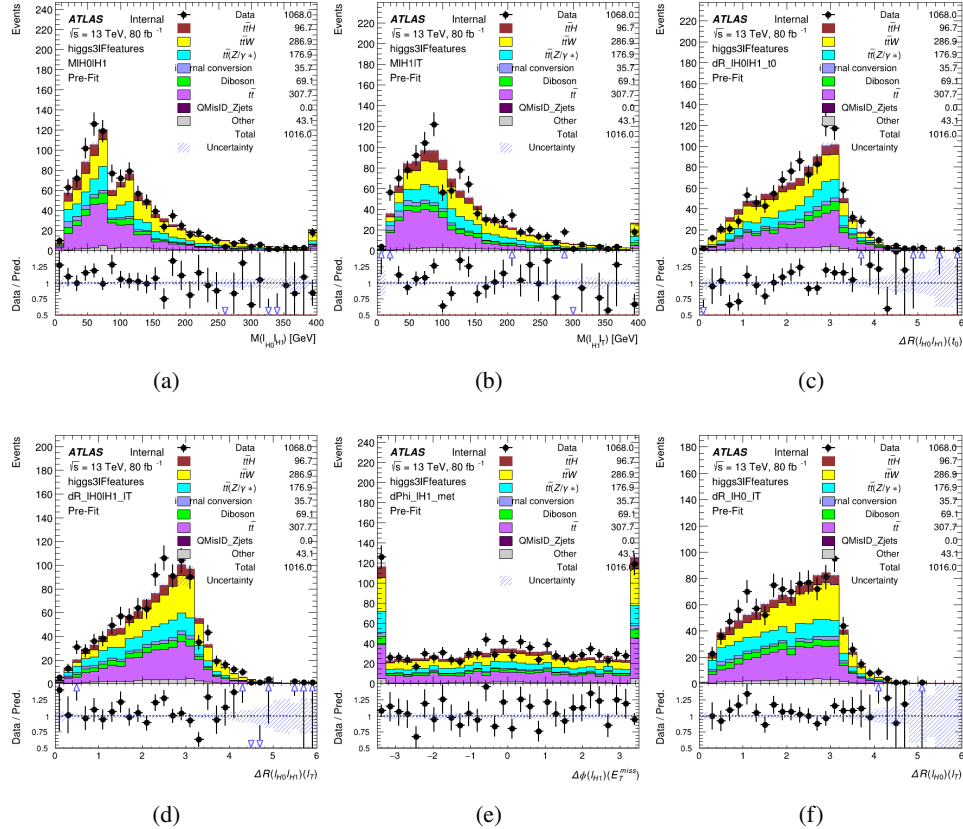


Figure 8.14: Data/MC comparisons of input features for higgs3IF training for 80 fb^{-1} of data.

567 are included as well, as these are found to improve performance. The truth p_T of the Higgs,
 568 as predicted by MC, are used as labels. Separate models are built for each channel - 2lSS, 3l
 569 Semi-leptonic and 3l Fully-leptonic.

570 As a two-bin fit is targeted for the final result, some metrics evaluating the performance
 571 of the models aim to show how well it distinguished between "high p_T " and "low p_T " events. A
 572 cutoff point of 150 GeV is used to define these two categories.

573 Because the analysis uses a two bin fit of the Higgs p_T , the momentum reconstruction

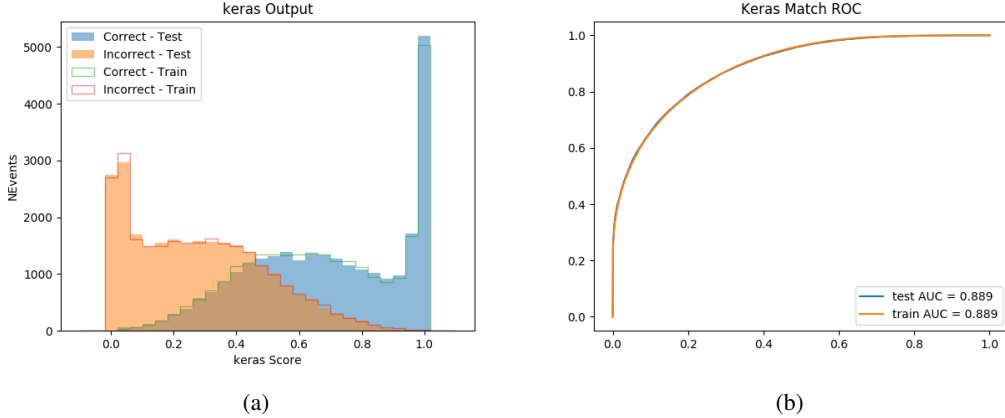


Figure 8.15: (a) the output score of the NN for correct and incorrect combinations of jets. (a) the ROC curve of the output, showing background rejection as a function of signal efficiency

574 could be treated as a binary classification problem, rather than a regression problem. This
 575 approach is explored in detail in section A.1.1, and is found not to provide any significant
 576 increase in sensitivity. The regression approach is used because it provides more flexibility
 577 for future analyses, as it is independent of the cutoff between high and low p_T , as well as the
 578 number of bins. Further, a regression allows the output of the neural network to be more clearly
 579 understood, as it can be directly compared to a physics observable.

580 **8.4.1 2ISS Channel**

581 The input variables listed in table ?? are used to predict the Higgs p_T in the 2ISS channel. Here
 582 j_0 and j_1 are the two jets identified as Higgs decay products. The lepton identified as originating
 583 from the Higgs is labeled l_H , while the other lepton is labeled l_T , as it most have come from the
 584 decay of one of the top quarks. The Higgs Reco Score and b-jet Reco Score are the outputs of
 585 the Higgs reconstruction algorithm, and the b-jet identification algorithm, respectively.

586 The optimal neural network architecture for this channel is found to consist of 5 hidden
 587 layers with 40 nodes each. The input data set includes 1.2 million events, 10% of which is used
 588 for testing, the other 90% for training. Training is found to converge after around 150 epochs.

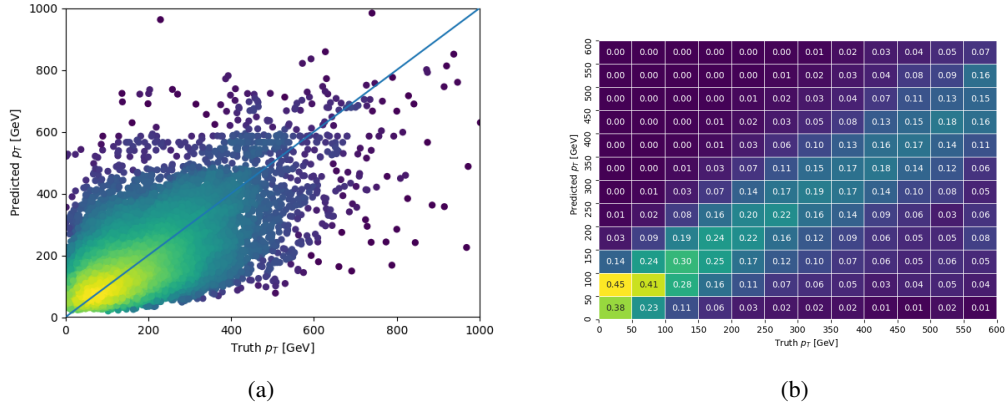


Figure 8.16:

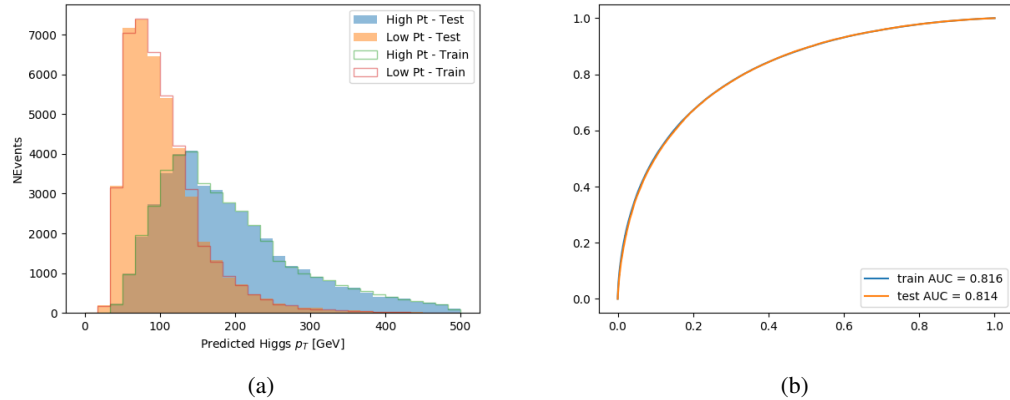


Figure 8.17:

589 8.4.2 3l Semi-leptonic Channel

590 The optimal neural network architecture for this channel is found to consist of 5 hidden
 591 layers with 40 nodes each. The input data set includes one million events, 10% of which is used
 592 for testing, the other 90% for training. Training is found to converge after around 150 epochs.

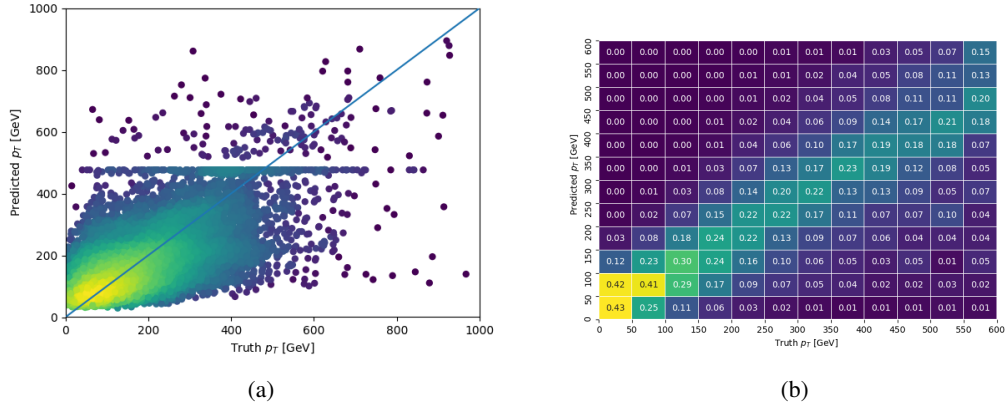


Figure 8.18:

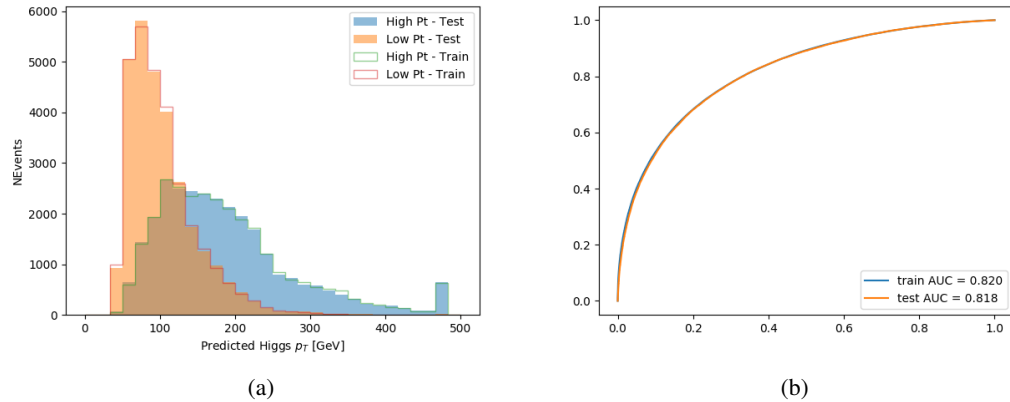


Figure 8.19:

593 8.4.3 3l Fully-leptonic Channel

594 The optimal neural network architecture for this channel is found to consist of 5 hidden
 595 layers with 40 nodes each. The input data set includes 400,000 events, 10% of which is used for
 596 testing, the other 90% for training. Training is found to converge after around 150 epochs.

597 The predicted transverse momentum, as a function of the truth p_T , is shown in figure ??.

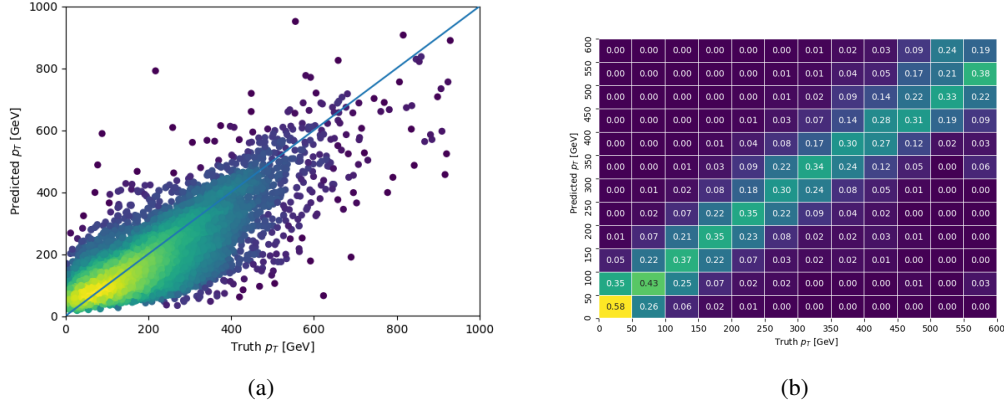


Figure 8.20:

598 When split into high and low p_T , based on a cutoff of 150 GeV, the

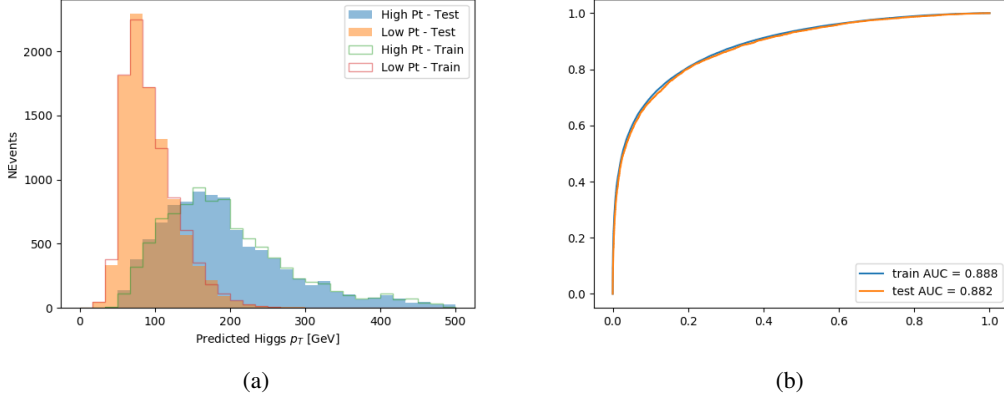


Figure 8.21:

599 8.5 3l Decay Mode

600 In the 3l channel, there are two possible ways for the Higgs to decay, both involving intermediate
601 W boson pairs: Either both W bosons decay leptonically, in which case the reconstructed decay
602 consists of two leptons (referred as the fully-leptonic 3l channel), or one W decays leptonically
603 and the other hadronically, giving two jets and one lepton in the final state (referred to as the
604 semi-leptonic 3l channel). In order to accurately reconstruct the Higgs, it is necessary to identify
605 which of these decays took place for each 3l event.

606 The kinematics of each event, along with the output scores of the Higgs and top recon-
607 struction algorithms, are used to distinguish these two possible decay modes. The particular
608 inputs used are listed in table ??.

609 A neural network with 5 hidden layers, each with 50 nodes, is trained to distinguish these
 610 two decay modes. The output of the model is summarized in figure 8.22.

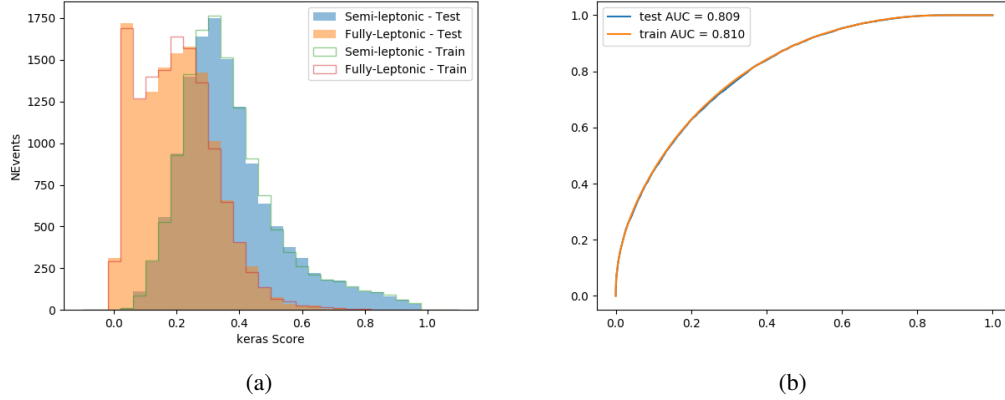


Figure 8.22:

611 9 Signal Region Definitions

612 Events are divided into two channels based on the number of leptons in the final state: one with
 613 two same-sign leptons, the other with three leptons. The 3l channel includes events where both
 614 leptons originated from the Higgs boson as well as events where only one of the leptons

615 9.1 Pre-MVA Event Selection

616 A preselection is applied to define orthogonal analysis channels based on the number of leptons
 617 in each event. For the 2lSS channel, the following preselection is used:

- 618 • Two very tight, same-charge, light leptons with $p_T > 20$ GeV

- 619 • $>=4$ reconstructed jets, $>=1$ b-tagged jets

- 620 • No reconstructed tau candidates

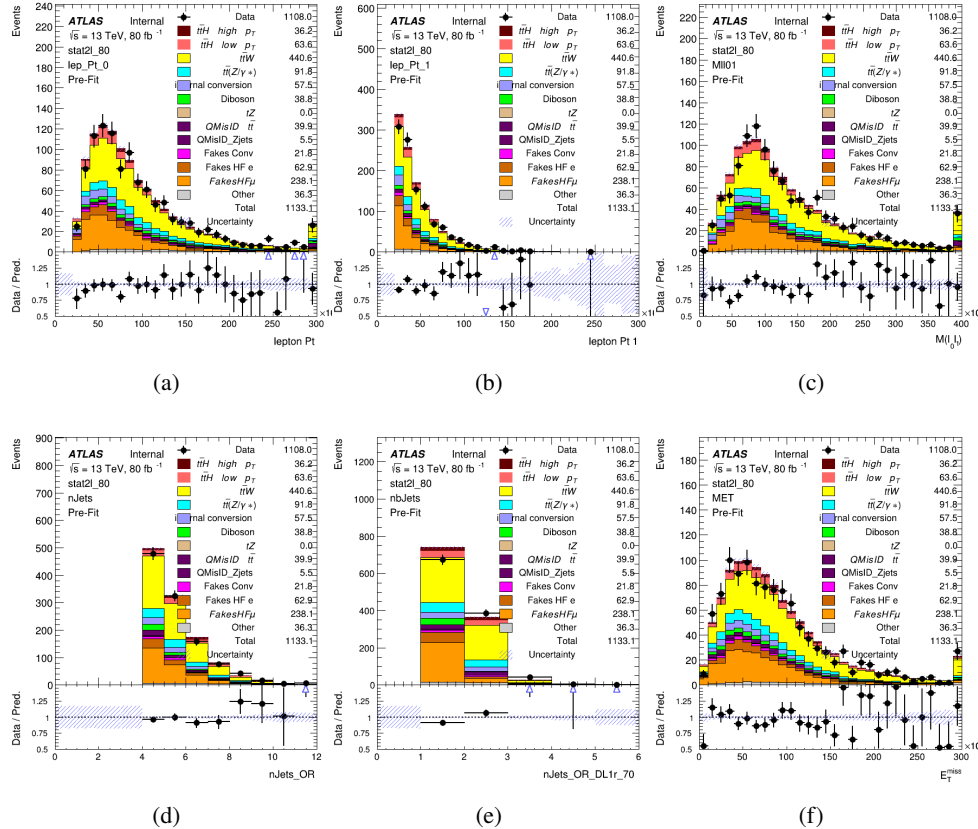


Figure 9.1:

621 For the 31 channel, the following selection is applied:

- 622 • Three light leptons with total charge ± 1
623 • Same charge leptons are required to be very tight, with $p_T > 20$ GeV

- 624 • Opposite charge lepton must be loose, with $p_T > 10 \text{ GeV}$

- 625 • $>=2$ reconstructed jets, $>=1$ b-tagged jets

- 626 • No reconstructed tau candidates

- 627 • $|M(l^+l^-) - 91.2 \text{ GeV}| > 10 \text{ GeV}$ for all opposite-charge, same-flavor lepton pairs

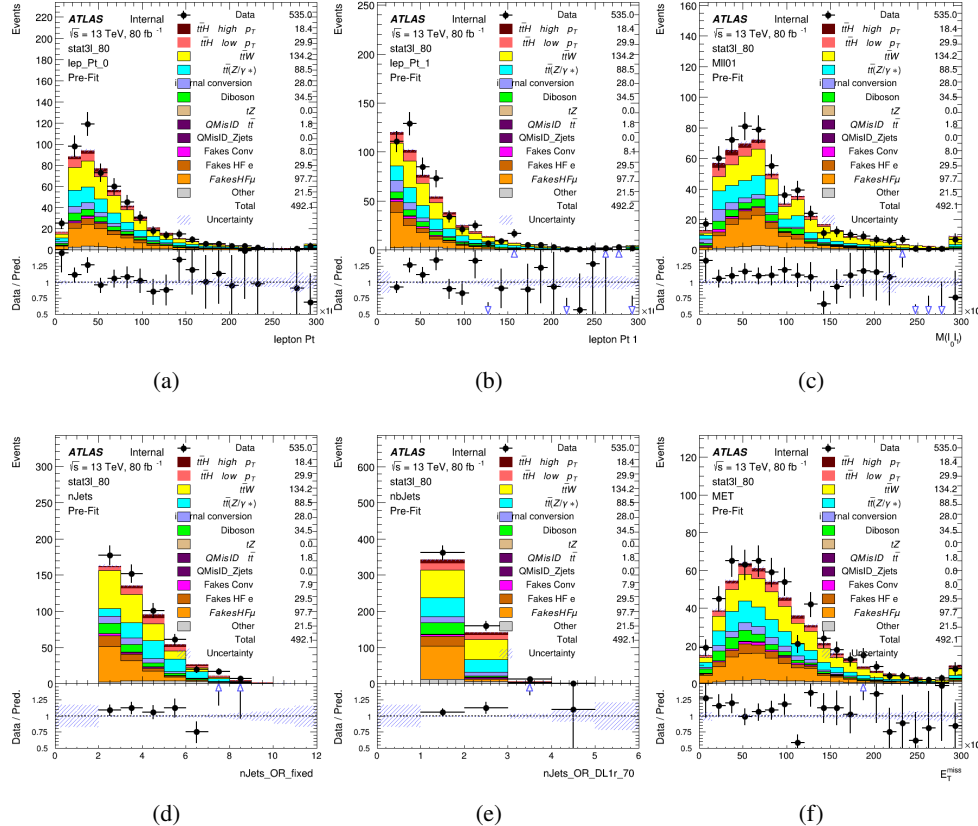


Figure 9.2:

628 9.2 Event MVA

629 Separate multi-variate analysis techniques (MVAs) are used in order to distinguish signal events
630 from background for each analysis channel - 2lSS, 3l semi-leptonic (3lS), and 3l fully leptonic
631 (3lF). In particular, Boosted Decision Tree (BDT) algorithms are produced with XGBoost
632 [xgboost] are trained using the kinematics of signal and background events derived from Monte
633 Carlo simulations. Events are weighted in the BDT training by the weight of each Monte Carlo
634 event.

635 Because the background composition differs for events with a high reconstructed Higgs p_T
636 compared to events with low reconstructed Higgs p_T , separate MVAs are produced for high and
637 low p_T regions. This is found to provide better significance than attempting to build an inclusive
638 model, as demonstrated in appendix A.1.3. A cutoff of 150 GeV is used. This gives a total of 6
639 background rejection MVAs - explicitly, 2lSS high p_T , 2lSS low p_T , 3lS high p_T , 3lS low p_T ,
640 3lF high p_T , and 3lF low p_T .

641 The following features are used in both the high and low p_T 2lSS BDTs:

HT	$M(\text{lep}, E_T^{\text{miss}})$	$M(l_0 l_1)$
binHiggs p_T 2lSS	$\Delta R(l_0)(l_1)$	diLepton type
higgsRecoScore	jet η 0	jet η 1
jet ϕ 0	jet ϕ 1	jet p_T 0
jet p_T 1	Lepton η 0	Lepton η 1
Lepton ϕ 0	Lepton ϕ 1	Lepton p_T 0
Lepton p_T 1	E_T^{miss}	$\min \Delta R(l_0)(\text{jet})$
$\min \Delta R(l_1)(\text{jet})$	$\min \Delta R(\text{Lepton})(\text{bjet})$	mjjMax frwdJet
nJets	nJets OR DL1r 60	nJets OR DL1r 70
nJets OR DL1r 85	signal	topRecoScore
weight		

Table 7: Input features

642

While for each of the 31 BDTs, the features listed below are used for training:

$M(\text{lep}, E_T^{\text{miss}})$	$M(l_0 l_1)$	$M(l_0 l_1 l_2)$
$M(l_0 l_2)$	$M(l_1 l_2)$	$\text{binHiggs } p_T \text{ 3lF}$
$\Delta R(l_0)(l_1)$	$\Delta R(l_0)(l_1)$	$\Delta R(l_0)(l_2)$
$\Delta R(l_1)(l_2)$	decayScore	higgsRecoScore3lF
higgsRecoScore3lS	$\text{jet } \eta \ 0$	$\text{jet } \eta \ 1$
$\text{jet } \phi \ 0$	$\text{jet } \phi \ 1$	$\text{jet } p_T \ 0$
$\text{jet } p_T \ 1$	$\text{Lepton } \eta \ 0$	$\text{Lepton } \eta \ 1$
$\text{Lepton } \eta \ 2$	$\text{Lepton } \phi \ 0$	$\text{Lepton } \phi \ 1$
$\text{Lepton } \phi \ 2$	$\text{Lepton } p_T \ 0$	$\text{Lepton } p_T \ 1$
$\text{Lepton } p_T \ 2$	E_T^{miss}	$\min \Delta R(l_0)(\text{jet})$
$\min \Delta R(l_1)(\text{jet})$	$\min \Delta R(l_2)(\text{jet})$	$\min \Delta R(\text{Lepton})(\text{bjet})$
$m_{jj} \text{Max frwdJet}$	$n\text{Jets}$	$n\text{Jets OR DL1r 60}$
$n\text{Jets OR DL1r 70}$	$n\text{Jets OR DL1r 85}$	signal
topScore	triLepton type	weight

Table 8: Input features

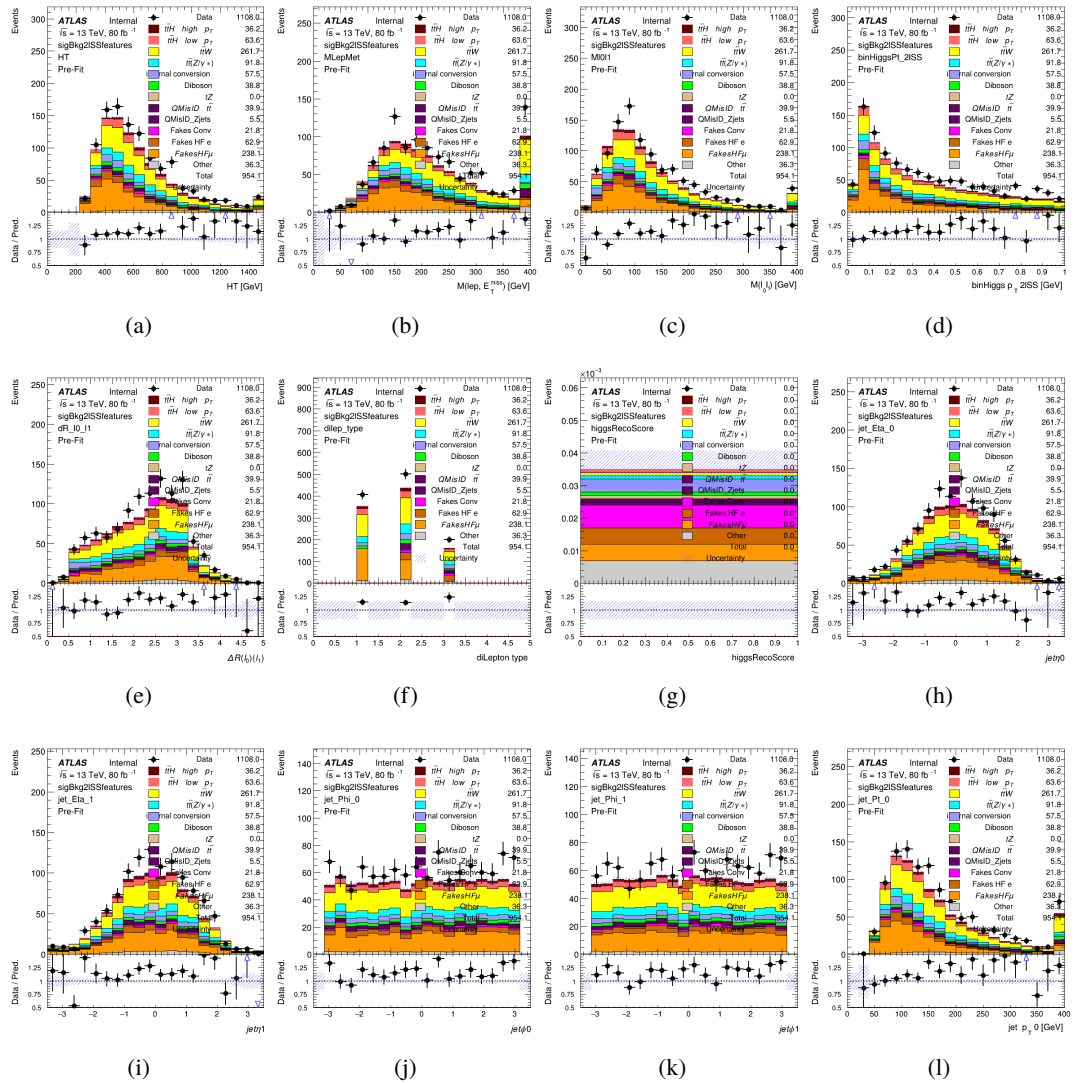


Figure 9.3:

643 The BDTs are produced with a maximum tree depth of 6, using AUC as the target loss
644 function.

645 Output distributions of each MVA are shown in figure 9.2.

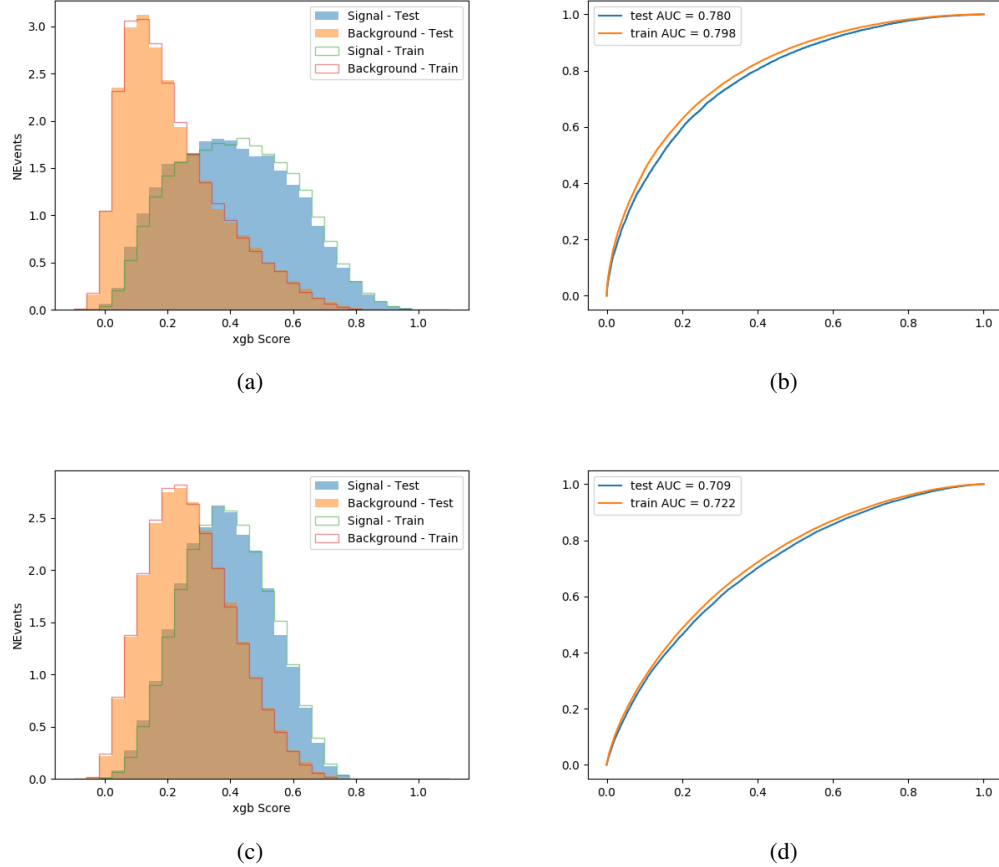


Figure 9.4:

646 9.3 Signal Region Definitions

647 Once pre-selection has been applied, channels are further refined based on the MVAs described
 648 above. The output of the model described in section 8.5 is used to separate the three channel
 649 into two - Semi-leptonic and Fully-leptonic - based on the predicted decay mode of the Higgs
 650 boson.

651 For each event, depending on the channel as well as the predicted p_T of the Higgs derived

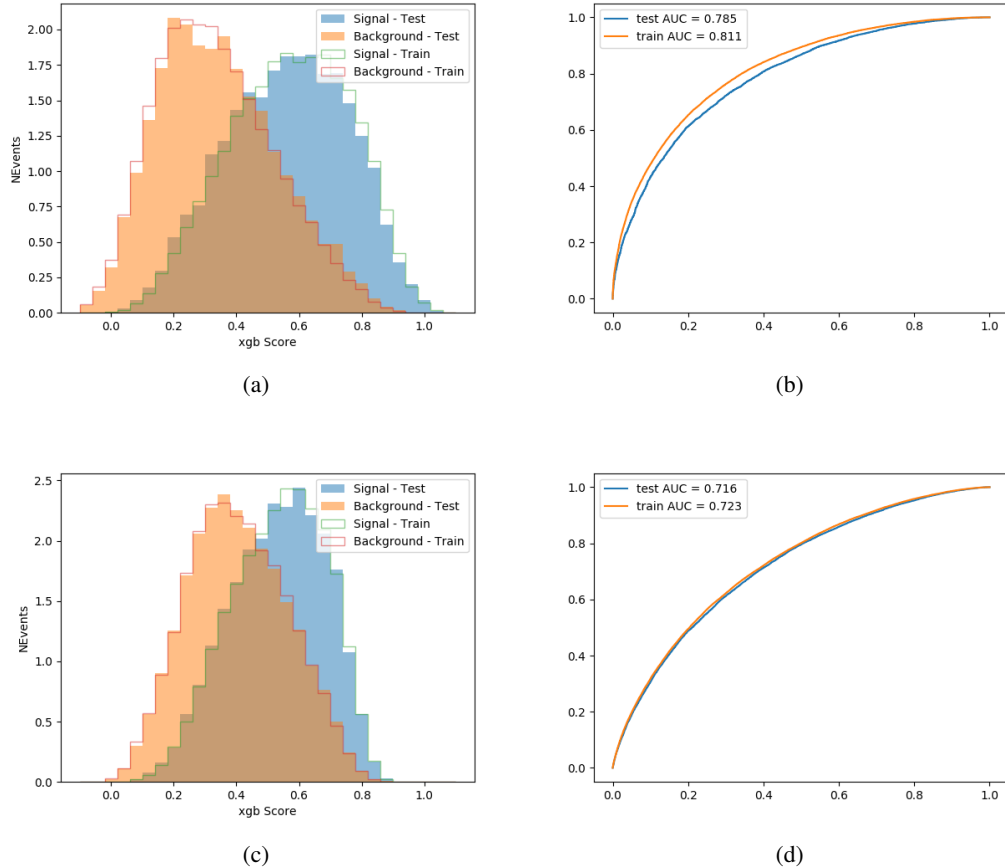


Figure 9.5:

from the algorithm described in section 8.4, a cut on the appropriate background rejection algorithm is applied. The specific selection used, and the event yield in each channel after this selection has been applied, is summarized below.

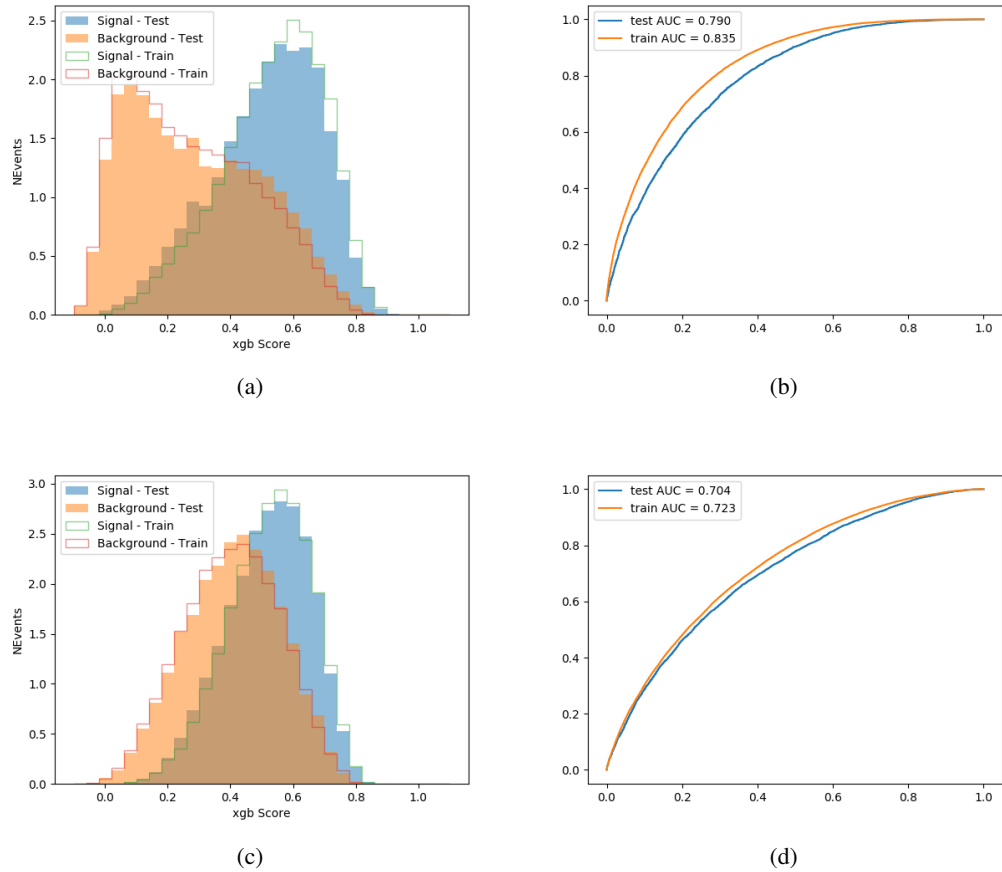


Figure 9.6:

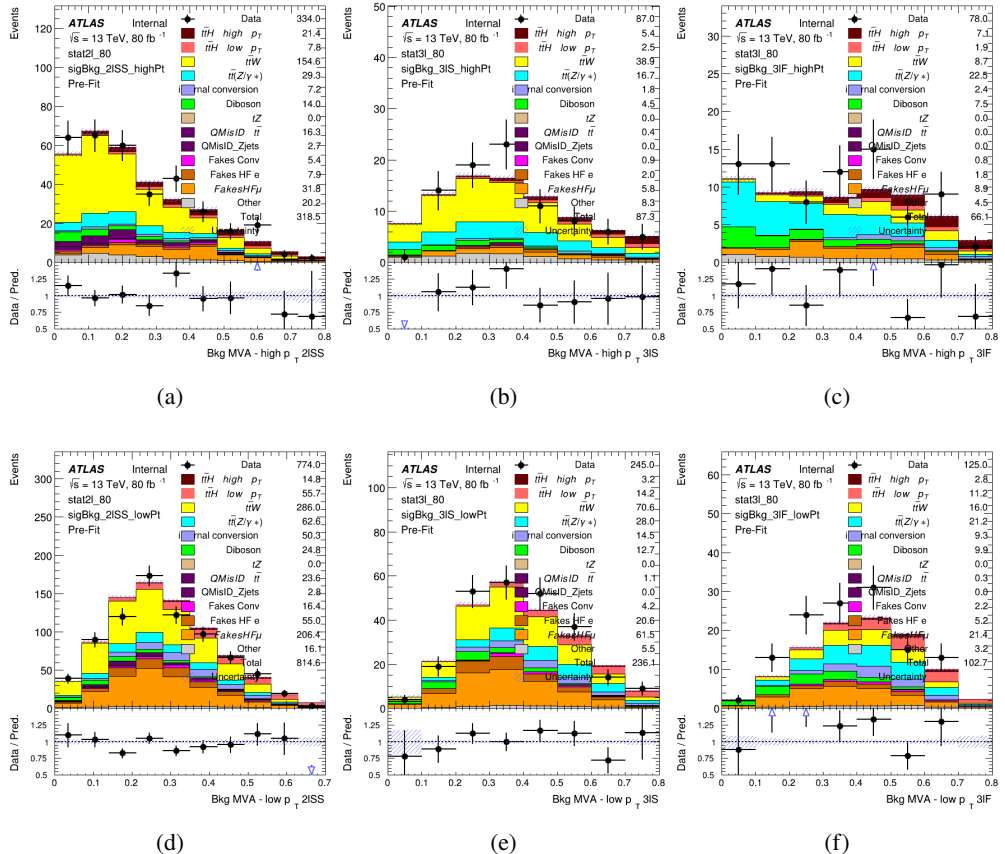


Figure 9.7: scores

655 9.3.1 2ISS

656 9.3.2 3l – Semi – leptonic

657 9.3.3 3l – Fully – leptonic

658 **10 Background Rejection MVA**

659 10.1 Background Rejection MVAs

660 Separate models are used in order to distinguish signal events from background for each analysis
9th November 2020 – 20:15 67
661 channel - 2lSS, 3l semi-leptonic, and 3l fully leptonic. In particular, Neural Networks produced

with Tensorflow are trained using the kinematics of signal and background events derived from Monte Carlo simulations. Further, because the background composition differs for events with a high reconstructed Higgs p_T compared to events with low reconstructed Higgs p_T , separate MVAs are produced for high and low p_T regions.

10.1.1 2lSS - High p_T

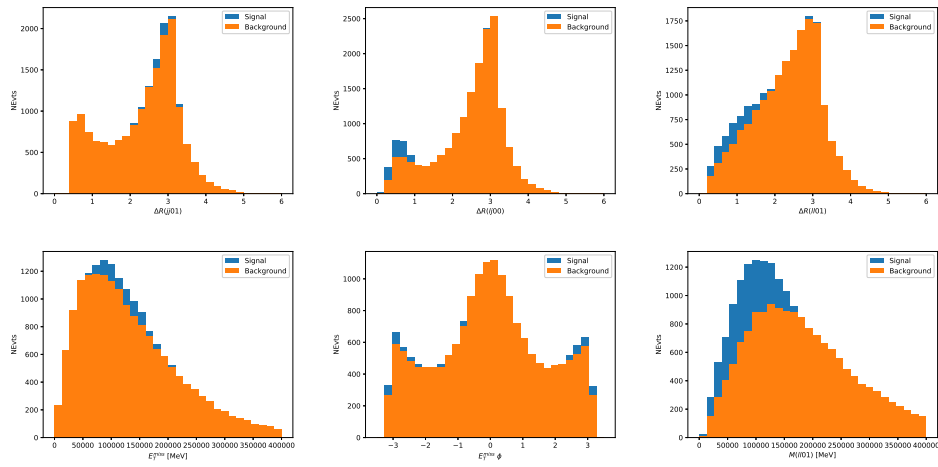


Figure 10.1:

667 **10.1.2 2lSS - Low p_T**

668 **10.1.3 3l Semi-Leptonic - High p_T**

669 **10.1.4 3l Semi-Leptonic - Low p_T**

670 **10.1.5 3l Fully Leptonic - High p_T**

671 **10.1.6 3l Fully Leptonic - Low p_T**

672 **11 Systematic Uncertainties**

673 The systematic uncertainties that are considered are summarized in table ???. These are imple-
674 mented in the fit either as a normalization factors or as a shape variation or both in the signal
675 and background estimations. The numerical impact of each of these uncertainties is outlined in
676 section 12.

677 The uncertainty in the combined 2015+2016 integrated luminosity is derived from a
678 calibration of the luminosity scale using x-y beam-separation scans performed in August 2015
679 and May 2016 [**lumi**].

680 The experimental uncertainties are related to the reconstruction and identification of light
681 leptons and b-tagging of jets, and to the reconstruction of E_T^{miss} . The sources which contribute

Table 9: Sources of systematic uncertainty considered in the analysis. Some of the systematic uncertainties are split into several components, as indicated by the number in the rightmost column.

Systematic uncertainty	Components
Luminosity	1
Pileup reweighting	1
Physics Objects	
Electron	6
Muon	15
Jet energy scale and resolution	28
Jet vertex fraction	1
Jet flavor tagging	131
E_T^{miss}	3
Total (Experimental)	186
Background Modeling	
Cross section	24
Renormalization and factorization scales	10
Parton shower and hadronization model	2
Shower tune	4
Total (Signal and background modeling)	40
Background Modeling	
Cross section	24
Renormalization and factorization scales	10
Parton shower and hadronization model	2
Shower tune	4
Total (Signal and background modeling)	40
Total (Overall)	226

682 to the uncertainty in the jet energy scale [`jes`] are decomposed into uncorrelated components and

683 treated as independent sources in the analysis.

684 The uncertainties in the b-tagging efficiencies measured in dedicated calibration analyses

685 [`btag_cal`] are also decomposed into uncorrelated components. The large number of components

686 for b-tagging is due to the calibration of the distribution of the BDT discriminant.

687 The systematic uncertainties associated with the signal and background processes are

688 accounted for by varying the cross-section of each process within its uncertainty.

689 12 Results

690 Unblinded results are shown for the 80 fb^{-1} data set, as well as MC only projections of results
 691 using the full Run-2, 140 fb^{-1} dataset.

692 12.1 Results - 80 fb^{-1}

693 A maximum likelihood fit is performed simultaneously over the regions shown in figure 12.1.

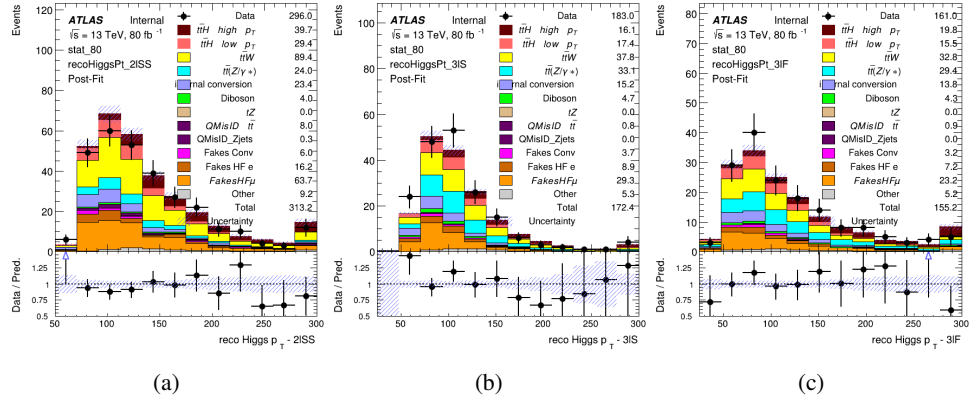


Figure 12.1:

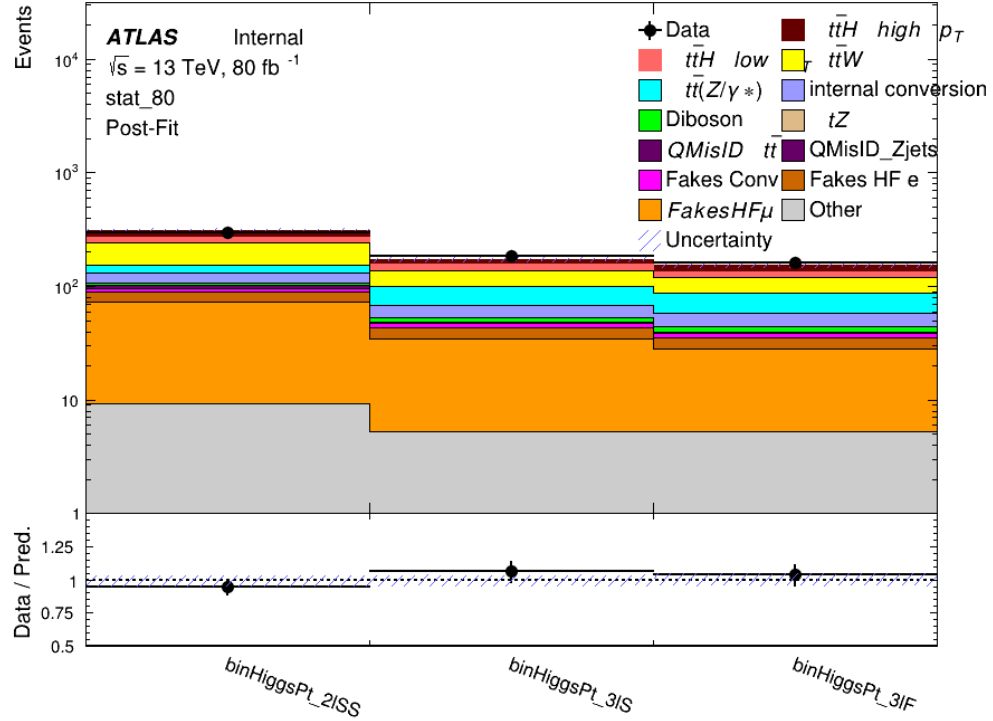


Figure 12.2: Post-fit summary of fit.

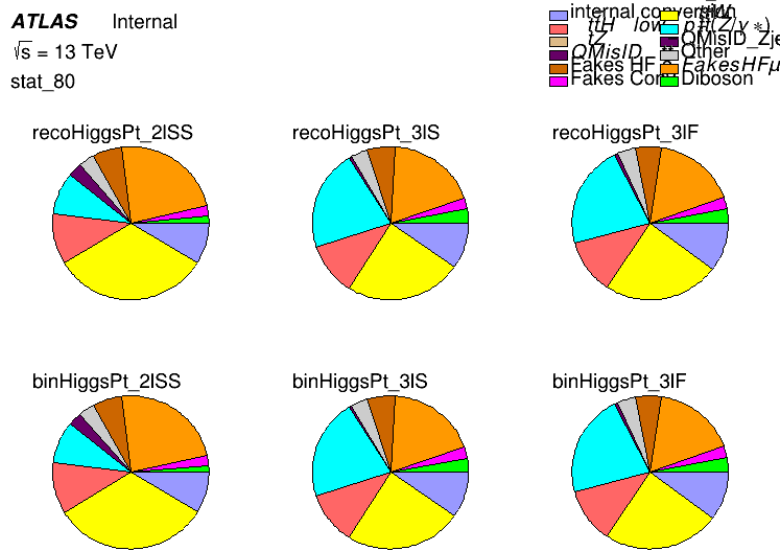


Figure 12.3: Background composition of the fit regions.

694 12.2 Projected Results - 140 fb^{-1}

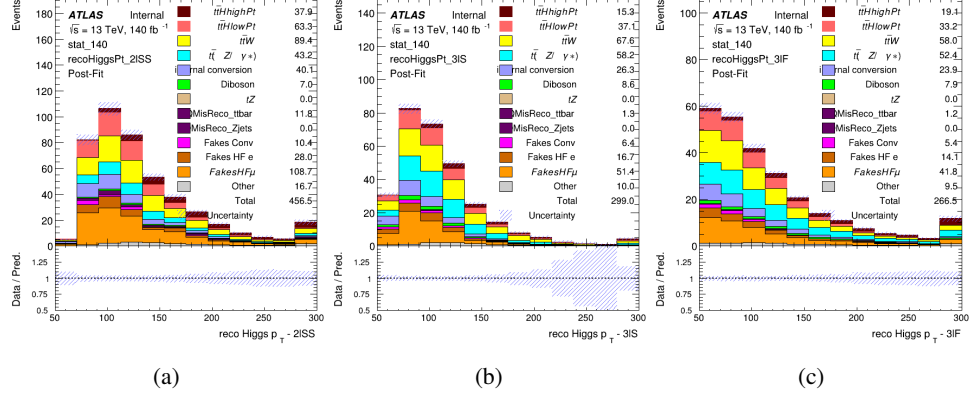


Figure 12.4:

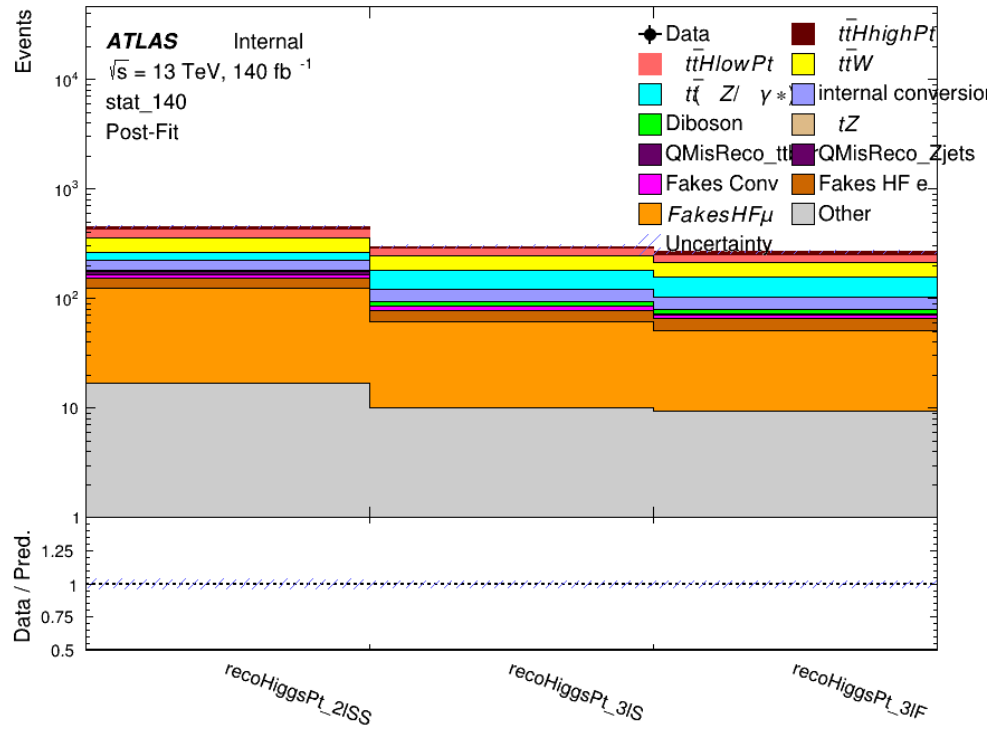


Figure 12.5: Post-fit summary of fit.

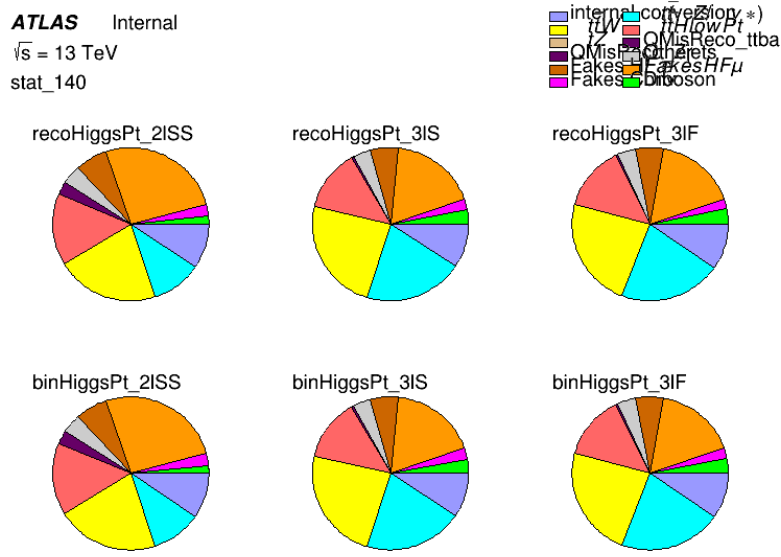


Figure 12.6: Background composition of the fit regions.

695 Part V

696 Conclusion

697 As search for the effects of dimension-six operators on $t\bar{t}H$ production is performed. An effective
 698 field theory approached is used to parameterize the effects of high energy physics on the Higgs
 699 momentum spectrum. The momentum spectrum is reconstructed using various MVA techniques,
 700 and the limits on dimension-six operators are limited to X.

⁷⁰¹ **List of contributions**

⁷⁰²

703 Appendices

704 A Machine Learning Models

705 The following section provides details regarding various studies performed in support of this
706 analysis, exploring alternate decisions and strategies.

707 A.1 Alternate b-jet Identification Algorithm

708 The nominal analysis reconstructs the b-jets by considering different combinations of jets, and
709 asking a neural network to determine whether each combination consists of b-jets from top quark
710 decays. An alternate approach would be to give the neural network about all of the jets in an event
711 at once, and train it to select which two are most likely to be the b-jets from top decay. It was
712 hypothesized that this could perform better than considering each combination independently, as
713 the neural network could consider the event as a whole. While this is not found to be the case,
714 these studies are documented here as a point of interest and comparison.

715 For these studies, the kinematics of the 10 highest p_T jets in each event are used for
716 training. This includes the vast majority of truth b-jets. Specifically the p_T , η , ϕ , E , and DL1r
717 score of each jet are used. For events with fewer than 10 jets, these values are substituted with 0.
718 The p_T , η , ϕ , and E of the leptons and E_T^{miss} are included as well.

719 Caterogical cross entropy is used as the loss function.

Table 10: Accuracey of the NN in identifying b-jets from tops in 2lSS events for the alternate categorical method compared to the nominal method.

Channel	Categorical	Nominal
2lSS		73.9%
3l		79.8%

720 A.1.1 Binary Classification of the Higgs p_T

721 A two bin fit of the Higgs momentum is used because statistics are insufficient for any finer
722 resolution. This means separating high and low p_T events is sufficient for this analysis. As
723 such, rather than attempting the reconstruct the full Higgs p_T spectrum, a binary classification
724 approach is explored.

725 A model is built to determine whether $t\bar{t}H$ events include a high p_T (>150 GeV) or low
726 p_T (<150 GeV) Higgs Boson. While this is now a classification model, it uses the same input
727 features described in section 8.4. Binary crossentropy is used as the loss function.

728 A.1.2 Impact of Alternative Jet Selection

729 A relatively low p_T threshold of 15 GeV is used to determine jet candidates, as the jets originating
730 from the Higgs decay are found to fall between 15 and 25 GeV a large fraction of the time. The
731 impact of different jet p_T cuts on our ability to reconstruct the Higgs p_T is explored here. The
732 performance of the Higgs p_T prediction models is evaluated for jet p_T cuts of 10, 15, 20, and 25
733 GeV.

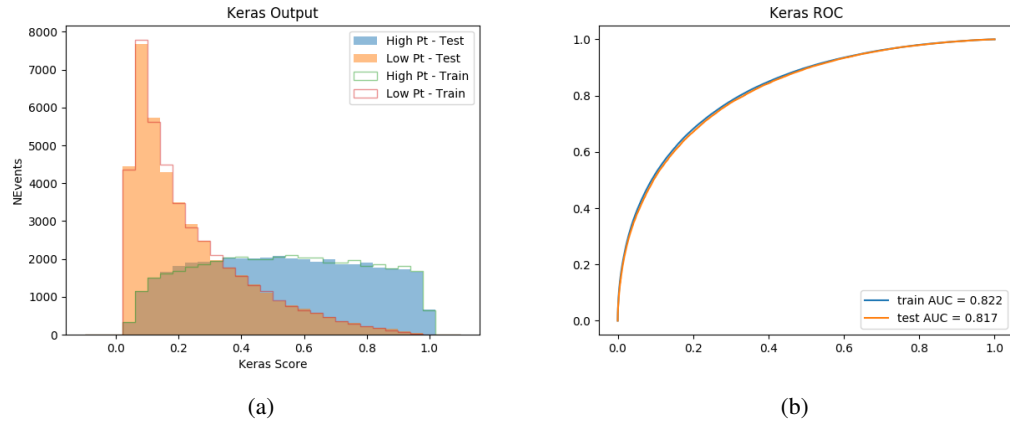


Figure A.1:

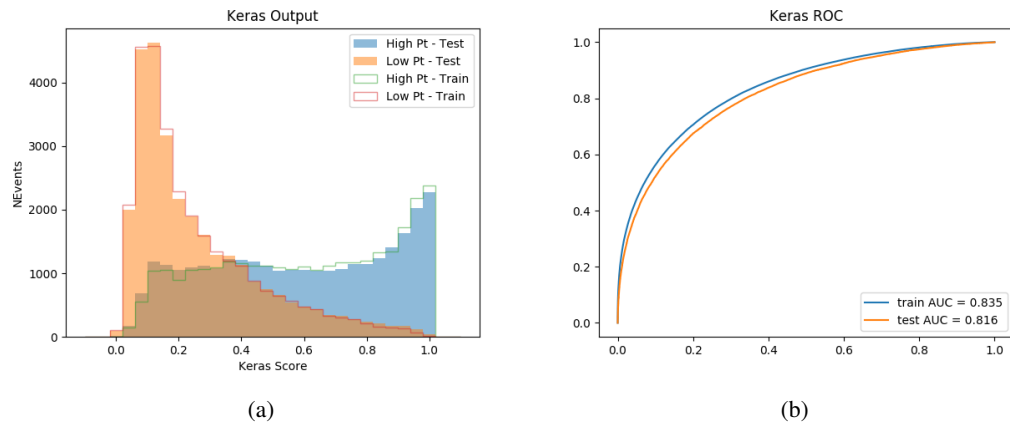


Figure A.2:

734 A.1.3 Background Rejection MVAs

735 **B**

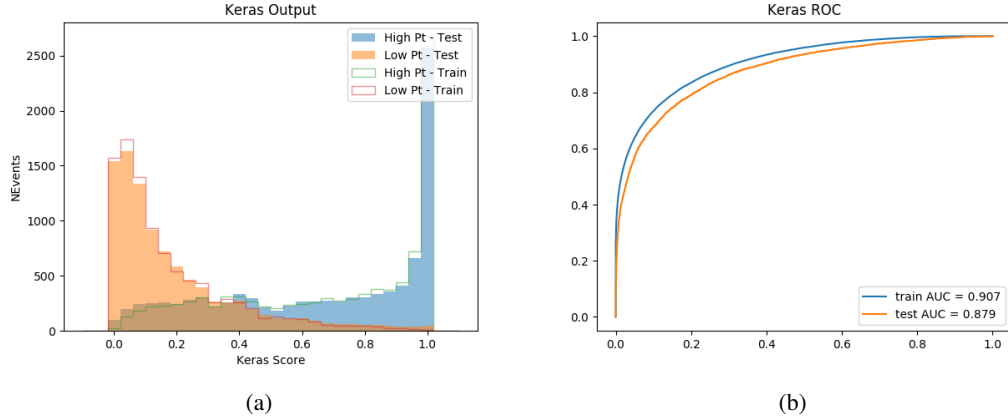


Figure A.3:

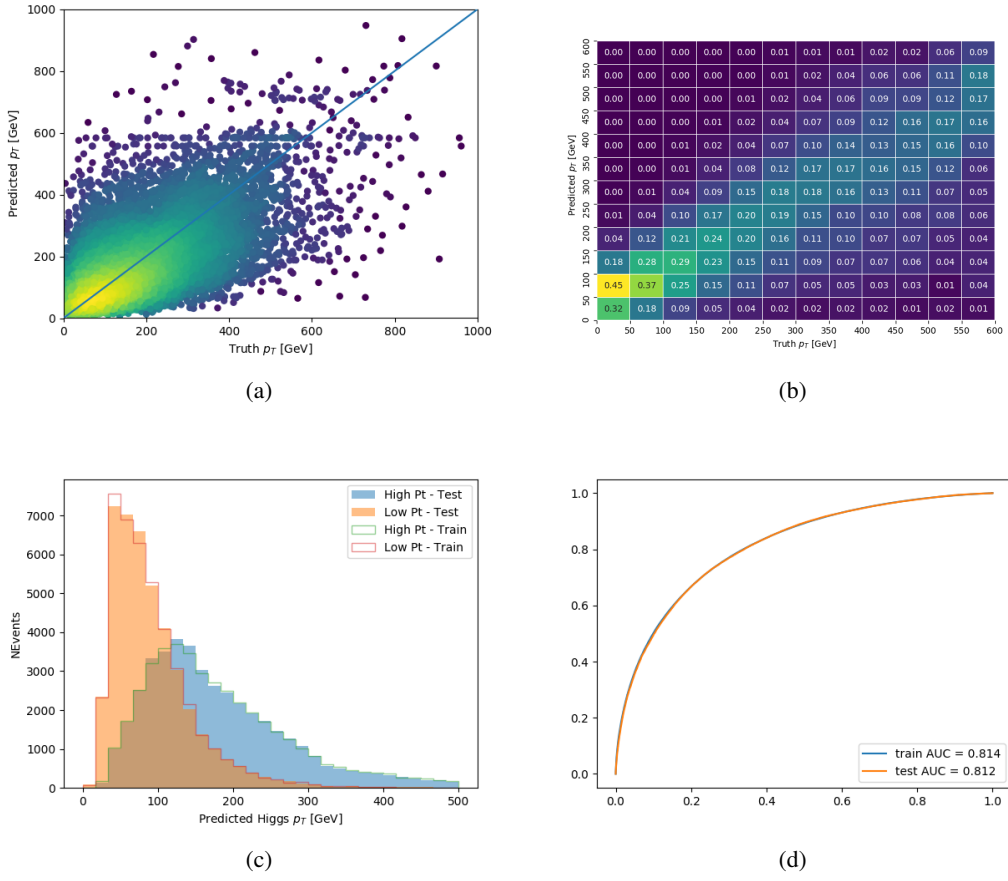


Figure A.4: